

UTRECHT UNIVERSITY
DEPARTMENT OF PHYSICS

Master's thesis in Climate Physics

**Tipping points in a conceptual model of AMOC-sea
ice interactions**

David Hokken

Supervisors:

dr. A. S. von der Heydt

dr. R. Bastiaansen

Second reader:

prof. dr. ir. H. A. Dijkstra

June 2022

Abstract

In the climate system, a variety of large-scale subsystems have been recognized as tipping elements: subsystems that feature critical thresholds beyond which they reorganize, often abruptly or irreversibly. Such tipping points are the subject of intense scrutiny as crossing them may have a profound environmental and societal impact. Tipping elements are frequently coupled; when one tips, it may bring another close to or past a critical threshold as well in a so-called tipping cascade. The variety in intrinsic timescales of the various coupled subsystems adds even further complexity. In this thesis, we use the mathematical framework of (nonlinear) dynamical system theory to study a conceptual model describing interactions between the Arctic sea ice cover and the Atlantic meridional overturning circulation that may have played a role in past Dansgaard-Oeschger events. This model features a two-way linear coupling between the (slowly evolving) oceanic temperature and (fast evolving) sea ice cover, reflecting both the insulating effect of sea ice on oceanic heat loss as well as oceanic forcing on sea ice. We utilize the difference in timescale through the theory of fast-slow systems to identify critical thresholds that are subsequently shown to exist in simulations. We find that a two-way and one-way linear coupling yield the same sort of tipping events. Furthermore, we demonstrate and discuss the existence of various types of cascading transitions within the system, including a rate-dependent cascading tipping point. This research suggests that both cascading and rate-dependent transitions may occur in the coupled AMOC-sea ice system, but that a comprehensive assessment of the boundaries of the basins of attraction – their movement, position with respect to the equilibria, and parameter dependence – is indispensable to assess the existence and timescales of rate-dependent tipplings and their likelihood to occur within a certain timeframe in this and more general coupled models.

Contents

Introduction	iv
1 Model description	1
1.1 The Stommel two-box model	1
1.2 Stommel box model: bifurcation analysis	5
1.3 The sea ice model	9
1.4 A coupled ocean-sea ice model	12
2 Fast-slow dynamics	14
2.1 Introduction	14
2.2 The reduced fast system	16
2.3 The reduced slow system	16
2.3.1 The slow manifold M_0^-	18
2.3.2 The slow manifold M_0^+	18
2.3.3 The case $c = 0$	20
2.4 Bifurcation structure as R varies	21
2.5 Nonautonomous version	23
3 Simulations	29
3.1 Testing the fast-slow analysis	29
3.2 Two examples of two transitions	31
3.3 Rate-dependent cascading tipping point	31
4 Discussion and conclusion	38
4.1 R-tipping and B-tipping	38
4.2 Classification of cascading tipping points	39
4.3 Interpretation of tippings	40
4.4 Conclusion and further research	40
A Supplementary material	42
Bibliography	43

Introduction

Tipping elements are components of the Earth’s climate system that are susceptible to tipping points: critical thresholds “beyond which the system reorganizes, often abruptly and/or irreversibly” [15, 19, 18]. Climate subsystems that have been identified as tipping elements include the Amazon rainforest, boreal forests, coral reefs, the Greenland and West Antarctic ice sheets, the Atlantic meridional overturning circulation (AMOC), and Arctic sea ice, many of which are presently out of equilibrium due to anthropogenic forcing [15, Ch. 2]. Since tipping elements do not exist in isolation but are often coupled, it has recently been suggested that tipping of one element could lead to tipping of another [6, 36, 26, 27], and the framework of such tipping cascades is currently topic of discussion [16]. In low-dimensional conceptual models, tipping points and cascades can be studied rigorously within the framework of (nonlinear) dynamical system theory [8]. Typically, critical thresholds are then represented by bifurcation points; even the tiniest shift of the bifurcation parameter beyond the bifurcation point causes the system to tip to an alternative, drastically different stable state. In state-of-the-art, high-dimensional climate models that have been used to investigate and catalogue possible tipping events in the (near) future, tipping is often less clear-cut [10]. This could point either at overtuning of such advanced models [29], underrepresentation of the relevant physical processes or spatial characteristics in conceptual models [4, 25], or both. At any rate, a robust assessment of critical thresholds can only be made by studying the relevant tipping elements across the modelling hierarchy [32, 9]. Conceptual models are the playground where possible mechanisms for tippings can be discerned and analyzed most easily.

In this thesis, we study a conceptual, bidirectionally coupled model incorporating dynamics of Arctic sea ice and the AMOC. Rapid loss of Arctic sea ice, which is taking place already [15, Ch. 9.3.1], exposes a larger part of the polar ocean to the atmosphere, leading to changes in the ocean-atmosphere heat exchange [12]. As more heat is lost to the atmosphere, Arctic ocean temperatures decline and the equator-to-pole temperature gradient increases, strengthening the AMOC. Although the AMOC is projected to weaken over the coming century [33], this mechanism may have played a role in past climate change. For example, Dansgaard-Oeschger (DO) events are thought to be linked to strengthening of

the AMOC, mediated through rapid loss of sea ice due to changes in wind patterns [20, 21, 14, 5].

Our bidirectionally coupled model is a slightly extended version of the AMOC-sea ice model introduced by Lohmann et al. [22] that tries to capture this mechanism. It features the Stommel box model as the ocean component [28] and a simplified version of the Arctic sea ice model by [12]. In [22], the components were coupled by a linear feedback of the sea ice into the ocean component, representing a change in atmospheric forcing of the polar ocean temperature due to changing sea ice cover (also described above). Our model includes an additional linear feedback of the polar oceanic temperature into the ice component, representing oceanic forcing on the sea ice.

We examine the tipplings and tipping cascades exhibited by the coupled model and investigate the underlying mechanisms. Tipping does not necessarily occur through a bifurcation (B-tipping): dynamical systems may also tip without reaching a (deterministic) bifurcation, but because noisy processes such as weather push the system far enough out of equilibrium (N-tipping). Furthermore, rate-induced tipping (R-tipping) occurs if the bifurcation parameter changes at a critical rate, even without necessarily attaining a critical threshold. In this case, the system cannot follow the moving stable state, as it changes too rapidly [3, 34, 35, 2, 24]. The mechanism explained above, by which a rapid decline of the sea ice cover leads to strenghtening of the AMOC, is captured by the model of Lohmann et al. [22] as an example of R-tipping.

In this work, we explore the parameter space of this model, creating an overview of possible tipplings and tipping cascades. For this, we employ the intrinsic difference in timescale between the (slowly evolving) ocean and the (fast evolving) sea ice to give a fast-slow analysis of the coupled system. We compare the tipping points and cascades in the two-way coupled model to those occurring in the unidirectionally coupled model of [22]. The mechanism of the rate-induced AMOC strenghtening following tipping of the ice cover is shown to persist in the bidirectionally coupled model as well; we investigate the circumstances under which they can occur. We also discuss the observed cascading tipplings in context of the classification made in [16].

This thesis is organized as follows. In Chapter 1, we describe the model components and their bifurcation structure, before presenting the full, coupled model used in this thesis. The fast-slow analysis of the coupled model is given in Chapter 2. In Chapter 3, results from the fast-slow analysis are compared to simulations. In addition, examples of cascading tipplings are discussed, including the rate-dependent cascading tipping point. A discussion of the results and conclusion is included in Chapter 4.

Acknowledgements

I would like to thank my supervisors Anna von der Heydt and Robbin Bastiaansen for their support and guidance throughout the year, in particular for the interesting discussions during our meetings and their insightful and extensive feedback on my writing.

Model description

In this chapter, we introduce the coupled AMOC-sea ice model that will be studied in this thesis. The model is a rescaled and slightly extended version of the one used in Lohmann et al. [22]. In §1.1 we introduce the ocean component, which is the well-known Stommel two-box model of the Atlantic thermohaline circulation [28]. A bifurcation analysis of the Stommel box model is given in §1.2. The sea ice component, described in §1.3, is taken from Eisenman and Wettlaufer [12, 11]. Finally, the coupled model is presented in §1.4.

1.1 The Stommel two-box model

Surface wind stress and large-scale spatial variations in the density of sea water set up pressure gradients that drive the global ocean circulation. Here, we focus on the density-driven part of the circulation. The density ρ of sea water is determined by temperature T and salinity S ; in deeper waters, pressure also plays an important role, but we will only be interested in the top layer of the ocean. The actual dependence of ρ on T and S is rather complicated and of high order, but the linear equation of state

$$\rho(T, S) = \rho_0(1 - \alpha(T - T_0) + \beta(S - S_0)) \quad (1.1)$$

is a decent approximation for the range of T and S values considered here [7, 30]. The symbols ρ_0 , T_0 and S_0 are reference values for density, temperature and salinity, and α and β are the thermal and haline expansion coefficients (see Table 1.1 for typical values). This equation captures two properties of seawater: its density increases when adding salt and decreases when adding heat. The water temperature is regulated by the atmosphere. Its salinity is determined by evaporation, precipitation and freshwater input. In the present-day climate, evaporation exceeds the combined effect of precipitation and freshwater input at low latitudes, and vice versa at high latitudes. Hence water is cold and fresh in the Arctic, and warm and salty at the equator.

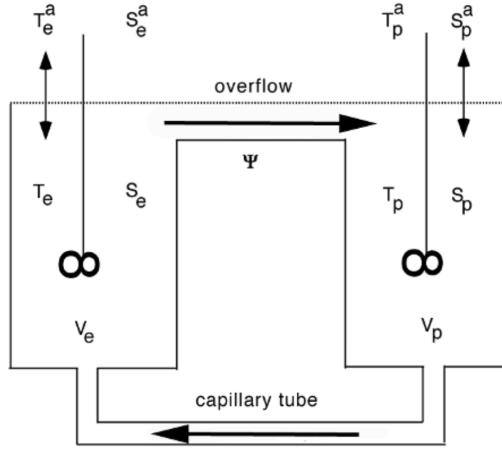


Figure 1.1: Sketch of the Stommel two-box model of the AMOC (taken from [7, p. 385]); the direction of the flow indicated here holds when the flow is dominated by the temperature gradient.

The thermohaline circulation is the idealized part of the global oceanic circulation driven solely by gradients in temperature and salinity. In the Atlantic ocean, warm and salty water is transported northwards at the surface. As it cools, its density becomes larger, and sinking occurs in certain parts of the North Atlantic. The poleward surface flow is compensated by an equatorward return flow in deeper regions of the ocean. The net zonally integrated meridional volume transport in the Atlantic ocean is called the Atlantic meridional overturning circulation (AMOC), and it is part of the global thermohaline circulation. In 1961, Stommel [28] studied a two-box model of the AMOC; here, we follow the description of the Stommel model supplied in [7, Ch. 16.2]. The model divides the Atlantic ocean into a tropical and a polar box – see Figure 1.1. Each box contains well-mixed water masses of a certain temperature T_{e*} , T_{p*} and salinity S_{e*} , S_{p*} (here, e stands for equatorial and p for polar, and the subscript $*$ is used to denote quantities that will be scaled later). The water masses conceptually represent the mixed (top) layer of the equatorial and Arctic oceans.

A capillary tube connects the two boxes at the bottom. It is assumed that the flow is directed from high to low density and that its rate Ψ_* is linearly related to the density difference via

$$\Psi_* = \gamma \frac{\rho_p - \rho_e}{\rho_0}. \quad (1.2)$$

Here, $\gamma > 0$ is a constant that can be obtained by fitting Ψ_* to observations. The flow rate Ψ_* is by definition positive if the water in the polar box is denser, i.e. if the flow in the capillary is directed toward the equator. It represents the strength of the exchange of water mass between the polar and equatorial boxes. The two boxes are connected by a region of

overflow at the surface to maintain constant volume in each of the boxes. According to (1.1), the density difference is

$$\rho_p - \rho_e = \rho_0(\alpha(T_{e^*} - T_{p^*}) - \beta(S_{e^*} - S_{p^*}))$$

and hence

$$\Psi_* = \gamma(\alpha(T_{e^*} - T_{p^*}) - \beta(S_{e^*} - S_{p^*})). \quad (1.3)$$

The relation (1.3) shows that the flow direction and rate are determined by a competition between the (weighted) temperature and salinity gradients. In the present-day climate, water in the Atlantic has a higher density at the pole than at the equator (i.e., the temperature gradient prevails over the salinity gradient in (1.1)).

Suppose that the equatorial and polar temperatures and salinities T_{e^*} , T_{p^*} , S_{e^*} and S_{p^*} relax toward atmospherically forced constant values $T_{e^*}^a$, $T_{p^*}^a$, $S_{e^*}^a$ and $S_{p^*}^a$, respectively, at rates C_p^T , C_e^T , C_p^S and C_e^S ; we assume $T_{e^*}^a > T_{p^*}^a$ and $S_{e^*}^a > S_{p^*}^a$ to mimic realistic forcing (see above). Denote by V_e and V_p the total volume of the water in the equatorial and polar box. Heat and salt from one box to another are imported and exported at rate $|\Psi_*|$. Hence the total heat and salt content of the boxes evolve over time as

$$\begin{cases} V_p \frac{dT_{p^*}}{dt_*} = C_p^T(T_{p^*}^a - T_{p^*}) + |\Psi_*|(T_{e^*} - T_{p^*}), \\ V_e \frac{dT_{e^*}}{dt_*} = C_e^T(T_{e^*}^a - T_{e^*}) - |\Psi_*|(T_{e^*} - T_{p^*}), \\ V_p \frac{dS_{p^*}}{dt_*} = C_p^S(S_{p^*}^a - S_{p^*}) + |\Psi_*|(S_{e^*} - S_{p^*}), \\ V_e \frac{dS_{e^*}}{dt_*} = C_e^S(S_{e^*}^a - S_{e^*}) - |\Psi_*|(S_{e^*} - S_{p^*}). \end{cases} \quad (1.4)$$

We assume that

$$R_T = \frac{C_p^T}{V_p} = \frac{C_e^T}{V_e} \quad \text{and} \quad R_S = \frac{C_p^S}{V_p} = \frac{C_e^S}{V_e}$$

are constants. This assumption means that polar and equatorial water temperature relax at the same rate per unit volume, and the same for salinity. The constants $\tau_T = R_T^{-1}$ and $\tau_S = R_S^{-1}$ can be thought of as timescales at which temperature and salinity relax to their atmospherically forced values. In reality, these timescales are quite different: the temperature of surface water adjusts quicker to the atmospheric temperature than salinity responds to precipitation and evaporation. This leads to the salt-advection feedback, that is crucial for the existence of multiple equilibria in the Stommel model [31]. Suppose that Ψ_* increases. Then more heat and salt are transported poleward. The influence of the added heat on the water density at the pole is damped rather strongly compared to that of the

added salt, because $\tau_T < \tau_S$. The polar ocean thus becomes denser, further strengthening the circulation.

We will now derive a nondimensional version of the system (1.4). Let $\xi = V_e/(V_e + V_p)$ denote the relative volume of the tropical box. Set

$$t_* = \frac{1}{R_T}t, \quad \Psi_* = \xi V_p R_T \Psi, \quad T_{e,p*} = \frac{\xi V_p R_T}{\alpha \gamma} T_{e,p}, \quad \text{and} \quad S_{e,p*} = \frac{\xi V_p R_T}{\beta \gamma} S_{e,p}.$$

Then (1.3) shows that

$$\Psi = (T_e - T_p) - (S_e - S_p).$$

When, in addition, the parameters $T_{e,p*}^a$ and $S_{e,p*}^a$ are scaled in the same way as $T_{e,p*}$ and $S_{e,p*}$, the equations in (1.4) transform to

$$\begin{cases} \frac{dT_p}{dt} = T_p^a - T_p + \xi |\Psi| (T_e - T_p), \\ \frac{dT_e}{dt} = T_e^a - T_e + (\xi - 1) |\Psi| (T_e - T_p), \\ \frac{dS_p}{dt} = \frac{R_S}{R_T} (S_p^a - S_p) + \xi |\Psi| (S_e - S_p), \\ \frac{dS_e}{dt} = \frac{R_S}{R_T} (S_e^a - S_e) + (\xi - 1) |\Psi| (S_e - S_p). \end{cases} \quad (1.5)$$

Define the parameters

$$\eta_1 = T_e^a - T_p^a, \quad \eta_2 = \frac{R_S}{R_T} (S_e^a - S_p^a), \quad \text{and} \quad \eta_3 = \frac{R_S}{R_T} = \frac{\tau_T}{\tau_S}. \quad (1.6)$$

The parameter η_3 is the ratio of the timescales at which temperature and salt relax toward their atmospherically forced values. Above, we already discussed that $\tau_T < \tau_S$, and thus $\eta_3 < 1$. The parameters η_1 and η_2 are the temperature and salinity forcing gradients. Typical values of the parameters η_1 , η_2 and η_3 are derived at the end of this section. The temperature and salinity gradients $T = T_e - T_p$ and $S = S_e - S_p$ satisfy the two equations

$$\begin{cases} \frac{dT}{dt} = \eta_1 - T - |T - S|T, \\ \frac{dS}{dt} = \eta_2 - \eta_3 S - |T - S|S, \end{cases} \quad (1.7)$$

by subtracting the first equation from the second, and the third from the fourth, respectively, in (1.5).

We will also shortly look at the coupled ocean-sea ice model where the equations for polar and tropical temperatures are kept separate; the resulting system of equations is then

$$\begin{cases} \frac{dT_p}{dt} = T_p^a - T_p + \xi|T_e - T_p - S|(T_e - T_p), \\ \frac{dT_e}{dt} = T_e^a - T_e + (\xi - 1)|T_e - T_p - S|(T_e - T_p), \\ \frac{dS}{dt} = \eta_2 - \eta_3 S - |T_e - T_p - S|S. \end{cases} \quad (1.8)$$

Lastly, we take a look at typical parameter values. We follow [7, p. 383] in taking $\eta_3 = 0.3$, with $R_T = 0.005 \text{ yr}^{-1}$. Taking $\rho_p - \rho_e = 4.0 \text{ kgm}^{-3}$ and $\rho_0 = 1.0 \times 10^3 \text{ kgm}^{-3}$ gives $\gamma = 3.8 \times 10^9 \text{ m}^3 \text{ s}^{-1} = 1.2 \times 10^{17} \text{ m}^3 \text{ yr}^{-1}$ when $\Psi_* = 15 \text{ Sv}$. We take $T_{e^*}^a = 20^\circ \text{C}$ and $T_{p^*}^a = -10^\circ \text{C}$. Combining this with the values of parameters in Table 1.1, we obtain

$$T_e^a = \frac{\alpha\gamma}{\xi V_p R_T} T_{e^*}^a = \frac{1.0 \times 10^{-4} \cdot 1.2 \times 10^{17}}{0.70 \cdot 0.33 \times 10^{17} \cdot 0.005} \cdot 20 = 2.1$$

and similarly $T_p^a = -1.0$. This gives $\eta_1 = T_e^a - T_p^a = 3.1$. For the salinity values, taking $S_{e^*}^a = 38$ and $S_{p^*}^a = 33$ implies

$$S_e^a = \frac{\beta\gamma}{\xi V_p R_T} S_{e^*}^a = \frac{7.6 \times 10^{-4} \cdot 1.2 \times 10^{17}}{0.70 \cdot 0.33 \times 10^{17} \cdot 0.005} \cdot 38 = 30$$

and similarly $S_p^a = 26$. This yields $\eta_2 = \eta_3(S_e^a - S_p^a) = 0.3 \cdot 4 = 1.2$.

From here on, we follow [7] in taking the default values $\eta_1 = 3.0$ and $\eta_2 = 1.0$.

1.2 Stommel box model: bifurcation analysis

In this section, we will give a brief bifurcation analysis of the Stommel two-box model given in (1.7). In equilibrium, the temporal derivatives on the left-hand side in (1.7) vanish. Therefore T and S can be written as

$$T = \frac{\eta_1}{1 + |T - S|} \quad \text{and} \quad S = \frac{\eta_2}{\eta_3 + |T - S|}; \quad (1.9)$$

note that the denominators are always positive. The flow strength $\Psi = T - S$ satisfies

$$\Psi = \frac{\eta_1}{1 + |\Psi|} - \frac{\eta_2}{\eta_3 + |\Psi|}$$

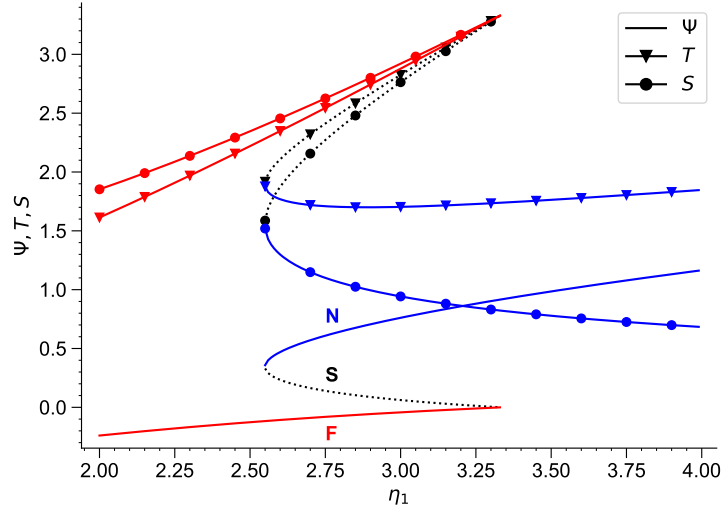


Figure 1.2: Bifurcation diagram of the ocean component (1.7) with respect to η_1 , with parameter values as in Table 1.1 and $\eta_2 = 1.0$, $\eta_3 = 0.3$. Each of Ψ , T and S are plotted. Solid (dotted) lines indicate stable (unstable) equilibrium points. The colored letters N, S and F indicate that the branches of that color are nodes, saddles, and foci.

which gives the equation

$$\Psi^3 + (1 + \eta_3)|\Psi|\Psi + (\eta_2 - \eta_1)|\Psi| + \eta_3\Psi + \eta_2 - \eta_1\eta_3 = 0 \quad (1.10)$$

after clearing denominators (note that $|\Psi|^2 = \Psi^2$). In other words, the quantity Ψ is a root of one of two distinct cubic equations, depending on its sign. Solutions to (1.10) lead to fixed points of T and S via (1.9); the real-valued ones are drawn in Figure 1.2, for varying atmospheric temperature forcing gradients η_1 . Notice that, for this choice of parameters, the poleward stable steady state flow (i.e., $T > S$) is much more vigorous than the salinity-driven equatorward flow, even though the temperature and salinity gradients are both larger in the latter regime.

A non-smooth bifurcation occurs at $\Psi = 0$, in which case we see from (1.10) that $\eta_2 = \eta_1\eta_3$. This means that the temperature and salinity forcing gradients are equal, and $T = S$; see (1.6).

In an equilibrium state (T^*, S^*) with $T^* \neq S^*$ and $\nu = \text{sign}(T^* - S^*)$, the Jacobian of (1.7) reads

$$J = \begin{pmatrix} -1 + \nu(S^* - 2T^*) & \nu T^* \\ -\nu S^* & -\eta_3 + \nu(2S^* - T^*) \end{pmatrix},$$

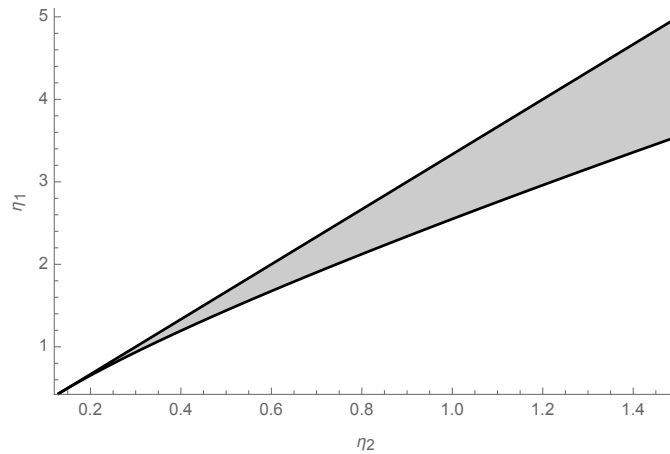


Figure 1.3: Bistability region (shaded) in terms of η_1 and η_2 for $\eta_3 = 0.3$.

whose trace $\text{tr}(J)$ satisfies

$$\text{tr}(J) = -1 - \eta_3 + 3\nu(S^* - T^*) = -1 - \eta_3 - 3|T^* - S^*| < 0.$$

In case $T^* = S^*$, we see again from (1.7) that the Jacobian is a diagonal matrix with entries -1 and $-\eta_3$, so its trace equals $-1 - \eta_3$. Since η_3 is positive, this means that the Jacobian has negative trace at every equilibrium point. Hence at least one eigenvalue of the Jacobian at each equilibrium point has negative real part. Moreover, this system cannot admit a Hopf bifurcation (as that would require a transition from a negative to a positive trace). However, unstable fixed points do exist for typical values of the parameters involved, which must thus be saddle points.

Figure 1.3 shows for which choice of values of η_1 and η_2 the Stommel model features bistability, given the fixed value $\eta_3 = 0.3$. The boundaries of the bistability regions are given by the bifurcation points of the Stommel system. The non-smooth bifurcation is visible at the straight boundary on the line $\eta_1 = \eta_2/\eta_3$. The other (curved) boundary represents the saddle-node bifurcation, which occurs exactly when the defining cubic equation (1.10) for Ψ in the region $\Psi > 0$ has a double root. This corresponds to a root of the polynomial discriminant of (1.10), which can be calculated algebraically with e.g. `Mathematica`. For $\eta_2 = 1.0$ and $\eta_3 = 0.3$, the saddle-node bifurcation occurs at $\eta_1 = \eta_1^{\text{sn}} \approx 2.549$, in which case $T = T^{\text{sn}} \approx 1.897$; see Figure 1.2.

The dynamics of the Stommel system can be represented by considering the phase space of the system. Figure 1.4 shows the stable equilibria for certain levels of η_1 that lie within the bistability region of the Stommel model when $\eta_2 = 1.0$ and $\eta_3 = 0.3$. An initial state (T_0, S_0) lies in the basin of attraction of the off-equilibrium if it converges to the

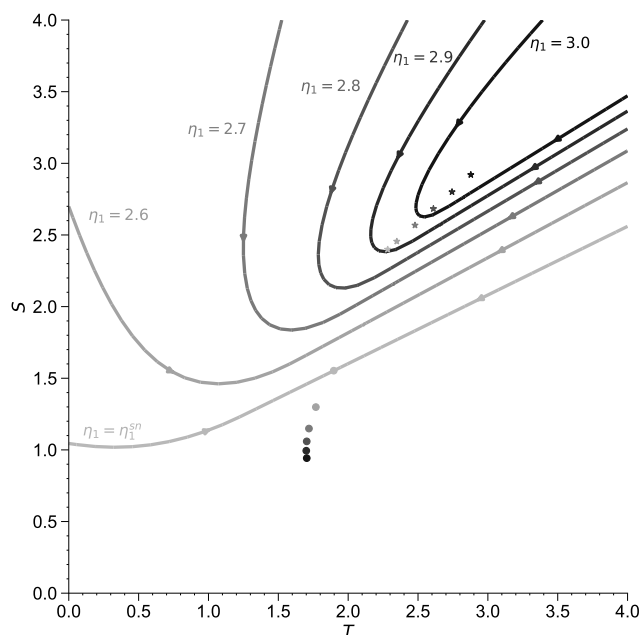


Figure 1.4: Basin boundary (curves) separating the basins of attraction of the on- and off-equilibria (dots and stars) of the Stommel model (1.7) as η_1 varies, with $\eta_2 = 1.0$ and $\eta_3 = 0.3$ fixed, in a T - S diagram. The shading indicates which equilibria correspond to which basin boundary.

off-state over time, and similarly for the on-state. The two basins of attraction are separated by the basin boundary (also shown in Fig. 1.4 for the various levels of η_1); if an initial state lies exactly on the basin boundary, it will converge to the unstable saddle equilibrium. It is also called the stable manifold of the saddle equilibrium. The basin boundaries in Figure 1.4 have been obtained by backward integration of the unstable saddle equilibrium. Here, we describe the movement of the basin boundary and its position relative to the equilibria, as that will be important later on. When $\eta_1 = \eta_1^{\text{sn}}$, the oceanic-on and the saddle equilibrium coincide. As η_1 increases, the basin of attraction of the on-state becomes larger and larger, and always contains the basin of attraction for smaller values of η_1 . This is called forward basin stability [35]. In particular, the on-equilibrium for $\eta_1 = \eta$ always lies in the basin of attraction of on-state for $\eta_1 > \eta$. For the off-state, this is not the case. Indeed, the off-equilibrium for $\eta_1 \leq 2.7$ does not lie within the basin of attraction of the off-state for $\eta_1 = 3.0$.

1.3 The sea ice model

The sea ice component of our model consists of a modification of the energy balance model introduced by Eisenman in [11] (E12 hereafter) for the surface enthalpy E_* of the Arctic ocean; it is the same model as the one used by Lohmann et al. [22]. To be more precise, the variable E_* represents the amount of energy stored in either (1) sea ice as latent heat when the ocean is ice-covered, or in (2) the ocean mixed layer as sensible heat when the ocean is ice-free. The two cases are separated by the sign of E_* , which is negative if the ocean is ice-covered and positive if it is ice-free. Before describing the model E12, let us briefly mention that it is approximately equivalent to the energy balance model (EW09 hereafter) first discussed in [12] and derived from the model in [23]; see [11, §2.1] for a comparison between the two models. Nondimensionally, the model E12 reads (see [11, §2.4])

$$\frac{dE_*}{dt} = A_* - BT_{sm*} + F_b$$

where all tildes are dropped, and we adopt the notation T_{sm*} instead of T in order not to confuse this temperature with the variable T from the preceding section. Here, the constant F_b represents a heat flux into the bottom of the model domain. That is, we can think of F_b as an energy flux transported toward the surface from deeper waters. The term $T_{sm*} = T_s - T_m$ represents the difference in temperature between the surface and the melting point of sea water; the term $A_* - BT_{sm*}$ represents the net surface energy flux (longwave and shortwave), with linearised dependence on T_{sm*} . However, the default parameter values also take sensible and latent heat fluxes into account.

Our model is obtained after applying a few alterations and simplifications to E12, all following [22]. The first simplification concerns the definition of A_* , which is in our case

$$A_* = \Delta_{a*} \tanh\left(\frac{E_*}{h_a}\right) + 1 - L_m.$$

The constants L_m and Δ_{a*} represent incoming longwave radiation and the difference in albedo between ocean and sea-ice, respectively. The first two terms together represent net shortwave radiation; the hyperbolic tangent is a smooth transition function between the ice-covered and ice-free regimes, with the parameter h_a determining the steepness of the transition in albedo. This A_* differs from \tilde{A} in [11, Eq. 10] in that it disregards seasonal effects (i.e. the terms involving cosines are ‘averaged out’).

Second, we partially linearize the model by setting $T_{sm*} = E_*$ (compare with the expression given in [11, Eq. (11)]). The partial linearisation discards nonlinear thermodynamic effects by which thinner sea ice grows faster. This is not done in [11], but is discussed for the model EW09; see [12, Eq. (2), (4), (5)]. Although the physical interpretation of the

bifurcation diagram is different after neglecting thermodynamic effects [12], its structure is essentially the same.

Third, we define our ice variable I_* as $I_* = -E_*$. An ice-covered ocean thus corresponds to a positive value of I_* . Furthermore, the exact value of I_* then represents the amount of energy stored in the Arctic sea ice. Denoting by \mathcal{H} the Heaviside function, we also add the term $R_0\mathcal{H}(I_*)I_*$ to model the export of sea ice, and a control parameter R_* . Both of these terms are also present in the model formulation in [12], but have been left out in [11]. This yields (recall that \tanh is an odd function)

$$\begin{aligned} \frac{dI_*}{dt} &= -A_* - BI_* - F_b + R_0\mathcal{H}(I_*)I_* + R_*, \\ &= -\Delta_{a*} \tanh\left(\frac{-I_*}{h_a}\right) - 1 + L_m - F_b - BI_* + R_0\mathcal{H}(I_*)I_* + R_*, \\ &= \Delta_{a*} \tanh\left(\frac{I_*}{h_a}\right) - 1 + L_m - F_b - BI_* + R_0\mathcal{H}(I_*)I_* + R_*, \end{aligned}$$

which is the sea ice component used in [22]. Following [22], we can think of the parameter R_* as representing influences on the sea ice volume due to external factors, such as added import or export of sea ice via alterations in the wind stress field. Alternatively, we could think of R_* as modelling climate change, for example by modulating the longwave radiation.

We scale our model further to reduce the number of parameters. Putting $I = I_*/h_a$ removes the (positive-valued) parameter h_a , and yields

$$h_a \frac{dI}{dt} = \Delta_{a*} \tanh(I) - 1 + L_m - F_b + (R_0\mathcal{H}(I) - B)h_a I + R_*.$$

Setting

$$R = (R_* - 1 + L_m - F_b)/h_a, \quad \Delta = \Delta_{a*}/h_a,$$

the equation for the sea ice component further simplifies to

$$\frac{dI}{dt} = \Delta \tanh(I) + (R_0\mathcal{H}(I) - B)I + R. \quad (1.11)$$

Typical values of all parameters involved can be found in Table 1.1; their derivation can be found in [11]. As we study a large ocean basin, we follow [22, Supplement, §1] in choosing the relatively large value $h_a = 0.5$. This contrasts with Eisenman's $h_a = 0.08$, which simulates the steep albedo transition at the ice edge. In addition, it is easier to detect critical slowing down of the ice variable for larger h_a , which is one of the goals in [22].

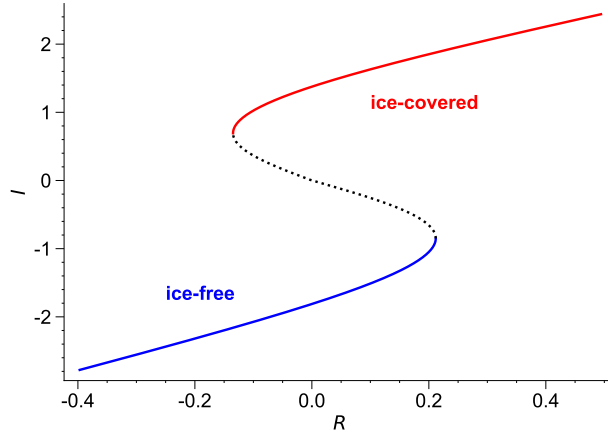


Figure 1.5: Bifurcation diagram of the sea ice component (1.11) with parameter values as in Table 1.1. Solid (dotted) lines indicate stable (unstable) fixed points. The parameter R is related to I according to (1.14).

Equilibria of the ice system (1.11) are found by equating the right-hand side to 0. Such an equilibrium is stable (unstable) if the derivative

$$\Delta \cosh^{-2}(I) + R_0 \mathcal{H}(I) - B \quad (1.12)$$

of the right-hand side in (1.11) with respect to I is negative (positive). Saddle-node bifurcations occur whenever the expression in (1.12) equals 0, i.e., when I equals

$$I_+^* = \cosh^{-1} \left(\sqrt{\frac{\Delta}{B - R_0}} \right) \approx 0.69 \quad \text{or} \quad I_-^* = -\cosh^{-1} \left(\sqrt{\frac{\Delta}{B}} \right) \approx -0.85 \quad (1.13)$$

(recall that $\cosh(x) = \cosh(-x)$; here, the positive branch is chosen for the inverse of \cosh). For any equilibrium value $I = I^*$ with $I_-^* < I < I_+^*$ the equilibrium is unstable. The bifurcation diagram is shown in Figure 1.5. Note that the pairs of values (R, I) in this figure satisfy the relation

$$-R = \Delta \tanh(I) + (R_0 \mathcal{H}(I) - B)I. \quad (1.14)$$

In particular, we define λ_+ and λ_- as the values of the right-hand side of (1.14) when $I = I_+^*$ and $I = I_-^*$, i.e.

$$\lambda_+ = \Delta \tanh(I_+^*) + (R_0 - B)I_+^* \approx 0.13 \quad \text{and} \quad \lambda_- = \Delta \tanh(I_-^*) - BI_-^* \approx -0.21. \quad (1.15)$$

These values will be needed in §2.3. Lastly, Lohmann et al. [22] defines the stadial state as the equilibrium ice value I_0^+ at $R_* = 0$, which in our rescaling corresponds to

$R = (-1 + L - F)/h_\alpha = 3/7$. This yields $I_0^+ \approx 2.312$. In general, our values of I are larger by a factor $1/h_\alpha$ (i.e., doubled; see Table 1.1) as compared to [22].

1.4 A coupled ocean-sea ice model

Sea ice acts as insulator of the Arctic ocean by preventing the water temperature T_p to relax toward (the lower value) T_p^a ; in other words, T_p^a is effectively increased by the presence of sea ice. In the coupled ocean-sea ice model, we take this into account, following [22], by replacing T_p^a with $T_p^a + \kappa \mathcal{H}(I)I$, where κ is some coupling constant. The Heaviside function \mathcal{H} is used because the insulation effect only takes place when sea ice is actually present in the system, i.e. $I > 0$. In contrast with the model in [22], ours also features a linear dependence of the growth of sea ice on T_p , reflecting that ice will develop quicker if T_p is lower. Combining these two couplings with (1.11) and (1.8), we obtain the coupled model

$$\begin{cases} \frac{dI}{dt} = \Delta \tanh(I) + (R_0 \mathcal{H}(I) - B)I + \tilde{c}T_p + R, \\ \tau_O \frac{dT_p}{dt} = T_p^a - T_p + \kappa \mathcal{H}(I)I + \xi |T_e - T_p - S|(T_e - T_p), \\ \tau_O \frac{dT_e}{dt} = T_e^a - T_e + (\xi - 1) |T_e - T_p - S|(T_e - T_p), \\ \tau_O \frac{dS}{dt} = \eta_2 - \eta_3 S - |T_e - T_p - S|S, \end{cases} \quad (1.16)$$

where $\tau_O = \tau_{\text{ocean}}/\tau_{\text{ice}}$ is the ratio of typical timescales of ocean and ice. Note that the value of \tilde{c} must be negative to model the effect of the polar oceanic temperature T_p on I realistically.

In order to reduce the number of state variables to only three, we make the further simplification of replacing the term $\tilde{c}T_p$ by cT , where $T = T_e - T_p$ and $c > 0$, i.e.

$$\begin{cases} \frac{dI}{dt} = \Delta \tanh(I) + (R_0 \mathcal{H}(I) - B)I + cT + R, \\ \tau_O \frac{dT}{dt} = \hat{\eta}_1 - \kappa \mathcal{H}(I)I - T - |T - S|T, \\ \tau_O \frac{dS}{dt} = \hat{\eta}_2 - \hat{\eta}_3 S - |T - S|S. \end{cases} \quad (1.17)$$

The hats on top of the η_i in (1.17) are introduced only to distinguish them from the η_i in the standard Stommel model (1.7), as we will compare the two systems later on. Although this simplification seems unjustified from a physical point of view (as it is unclear why ice growth would be affected by changes in the equator-to-pole temperature gradient), we

Table 1.1: Parameter values in the coupled ocean-sea ice models (1.16) and (1.17).

Characteristic	Notation	Default value	Source
Thermal expansion coefficient	α	$1.0 \times 10^{-4} \text{ K}^{-1}$	[7, p. 20]
Haline expansion coefficient	β	7.6×10^{-4}	[7, p. 20]
Volume of equatorial box	V_e	$0.78 \times 10^{17} \text{ m}^3$	[1, Tab. 1]
Volume of polar box	V_p	$0.33 \times 10^{17} \text{ m}^3$	[1, Tab. 1]
Relative volume of equatorial box	ξ	0.70	[1, Tab. 1]
Temperature forcing gradient	$\hat{\eta}_1$	3.0	[7, Ch. 16.2]
Salinity forcing gradient	$\hat{\eta}_2$	1.0	[7, Ch. 16.2]
Temperature-salinity timescale ratio	$\hat{\eta}_3$	0.3	[7, Ch. 16.2]
Ocean-sea ice albedo difference	Δ_{a^*}	0.43	[11, Tab. 1]
Albedo transition smoothness	h_a	0.5	[22, Tab. 1]
Sea ice export	R_0	-0.1	[22, Tab. 1]
Outgoing longwave radiation coeff.	B	0.45	[11, Tab. 1]
Incoming longwave radiation	L_m	1.25	[11, Tab. 1]
Ocean forcing on sea ice	F_b	$1/28 \approx 0.036$	[22, Tab. 1]
Sea ice-to-temperature coupling coeff.	κ	$0.151 \approx 0.35/I_0^+$	[22, Tab. 1]
Ocean-to-sea ice timescale ratio	τ_O	200	[22, Tab. 1]

will see in §3.3 that the behaviour of (1.17) and (1.16) might not be so different. This is ascribed to a relatively slow response of T_e compared to T_p to changes in I .

Although the coupled model described by the equations (7), (8) and (9) of [22] is the same as (1.17), further rescaling has been applied in the latter, so that the value $\kappa = 0.303$ in [22] correspond to our $\kappa = 0.151$.

Fast-slow dynamics

In this chapter, we study the coupled ocean-sea ice system (1.17) from the point of view of the theory of fast-slow systems [17], which is introduced in §2.1. In §2.2 and §2.3 we study the reduced fast and reduced slow system separately, leading to an overview of the bifurcation structure of the slow flow in §2.4 as a function of c and R (see Fig. 2.5 and Fig. 2.6). In §2.5 we discuss how a nonautonomous version of (1.17), where R varies in time, could alter the results obtained from the fast-slow analysis.

2.1 Introduction

The parameter τ_O in (1.17) represents the ratio of timescales of ocean and sea ice, i.e. $\tau_O = \tau_{\text{ocean}}/\tau_{\text{ice}}$. In reality, the ocean timescale is much larger than that of sea ice, as the response of the sea ice cover to forcing is typically much quicker than that of temperature and salinity of the ocean ([13] gives $\tau_O = 33$, but we stick with $\tau_O = 200$ as in [22]). Hence the parameter ϵ defined as $\epsilon = \tau_O^{-1} \ll 1$ is small. The coupled ocean-sea ice system (1.17) is thus an example of a fast-slow system, where I is the fast variable and T and S are the slow variables. In this chapter, we employ the theory of fast-slow systems to analyse it.

With

$$f(I, T) = \Delta \tanh(I) + (R_0 \mathcal{H}(I) - B)I + cT + R, \quad (2.1)$$

$$g_1(I, T, S) = \hat{\eta}_1 - \kappa \mathcal{H}(I)I - T - |T - S|T, \quad (2.2)$$

$$g_2(T, S) = \hat{\eta}_2 - \hat{\eta}_3 S - |T - S|S, \quad (2.3)$$

the fast system of (1.17) reads

$$\begin{cases} I' = f(I, T), \\ T' = \epsilon g_1(I, T, S), \\ S' = \epsilon g_2(T, S), \end{cases} \quad (2.4)$$

where the derivatives are with respect to the fast timescale t , and the slow system is

$$\begin{cases} \epsilon \dot{I} = f(I, T), \\ \dot{T} = g_1(I, T, S), \\ \dot{S} = g_2(T, S), \end{cases} \quad (2.5)$$

where the derivatives are with respect to the slow timescale $\tau = \epsilon t$. Away from $\epsilon = 0$, these systems are equivalent. In the singular limit $\epsilon = 0$, we obtain the reduced fast system

$$\begin{cases} I' = f(I, T), \\ T' = S' = 0, \end{cases} \quad (2.6)$$

from (2.4) and the reduced slow system

$$\begin{cases} 0 = f(I, T), \\ \dot{T} = g_1(I, T, S), \\ \dot{S} = g_2(T, S), \end{cases} \quad (2.7)$$

from (2.5). Knowledge on the fast and slow reduced systems can be combined using Fenichel's invariant manifold theorems to say something about the full, unreduced system (2.4) where ϵ is positive but sufficiently small. Let us give a short explanation of the first of these theorems in the current context. First, notice that equilibria of the reduced fast system are encoded in

$$C_0 = \{(I, T, S) \in \mathbb{R}^3 \mid f(I, T) = 0\}, \quad (2.8)$$

called the critical set. At the same time, the slow flow - i.e. the flow prescribed by the reduced slow system - also takes place on the critical set. Suppose $M_0 \subset C_0$ is a manifold with the property that it is normally hyperbolic everywhere in its domain, i.e. that $\partial f / \partial I$ does not vanish. Then Fenichel's first invariant manifold theorem ensures, for each sufficiently small ϵ greater than zero, the existence of a manifold M_ϵ that lies 'very close to' M_0 , is 'very similar to' M_0 , and where the unreduced flow of (2.4) takes place (see [17, Thm. 3.1.4] for precise statements). Thus, by studying the flow on M_0 , we can gain information about the fully coupled system for small, positive ϵ , which is what ultimately interests us. In this chapter, we determine the two slow manifolds M_0^+ and M_0^- corresponding to a stable ice-covered and a stable ice-free state of the polar ocean and study the flow on them. In Chapter 3, we compare the theoretical results obtained in this chapter to simulations of the full, coupled model (1.17).

2.2 The reduced fast system

The reduced fast system (2.6) is the ice equation $I' = f(I, T)$, where T is treated as a constant parameter. In other words, it is parametrised by $\hat{R} = R + cT$. Equilibria of the reduced fast system satisfy

$$-\hat{R} = \Delta \tanh(I) + (R_0 \mathcal{H}(I) - B)I. \quad (2.9)$$

To assess the reduced fast system, we must establish where these equilibria lose their stability. This depends on the sign of

$$\frac{\partial f}{\partial I} = \Delta \cosh^{-2}(I) + R_0 \mathcal{H}(I) - B. \quad (2.10)$$

Because T (or more accurately, the terms involving T) in the ice equation do not depend on I , the right-hand side in (2.10) equals the expression in (1.12). In particular, it is independent of T and c . The values $I = I_+^* \approx 0.69$ and $I = I_-^* \approx -0.85$ (see (1.13)) at the bifurcation points of the uncoupled ice model discussed in §1.3 thus persist in the fully coupled model (1.17). The bifurcation diagram of the reduced fast system is simply equal to the bifurcation diagram of the ice component shown in Figure 1.5, but with R replaced by \hat{R} (i.e. the bifurcation diagram is shifted to the left by the positive value cT).

2.3 The reduced slow system

In the reduced slow system, the Stommel-like slow flow

$$\begin{cases} \dot{T} = g_1(I, T, S) = \hat{\eta}_1 - \kappa \mathcal{H}(I)I - T - |T - S|T, \\ \dot{S} = g_2(T, S) = \hat{\eta}_2 - \hat{\eta}_3 S - |T - S|S \end{cases} \quad (2.11)$$

is subject to the additional, algebraic constraint $f(I, T) = 0$, i.e.

$$-cT = \Delta \tanh(I) + (R_0 \mathcal{H}(I) - B)I + R. \quad (2.12)$$

The slow flow thus evolves on the critical set C_0 defined in (2.8), as we saw already in §2.1. Recall that Fenichel's first invariant manifold theorem only applies to a manifold $M_0 \subset C_0$ that is normally hyperbolic, which here means that $\partial f / \partial I$ does not vanish. In §2.2, we concluded that $\partial f / \partial I \neq 0$ holds away from the two bifurcation points $I = I_+^*$ and $I = I_-^*$. Since we will restrict our attention to the stable states, the maximal normally

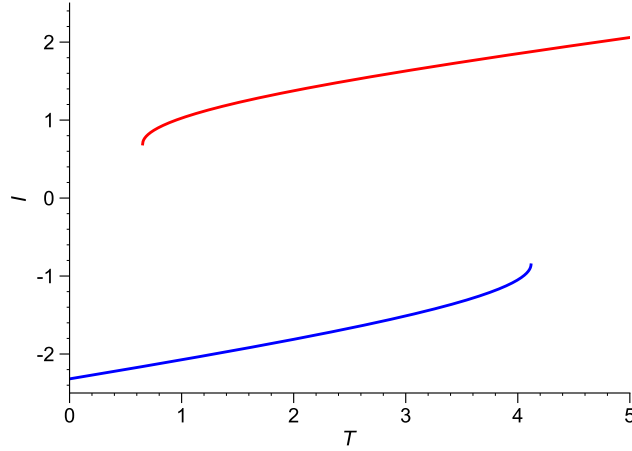


Figure 2.1: The functions $I_+(T)$ (red) and $I_-(T)$ (blue) for $R = -0.2$ and $c = 0.1$. The thresholds $T_+(R)$ and $T_-(R)$ are the minimum and maximum values attained by $I_+(T)$ and $I_-(T)$, respectively.

hyperbolic subsets of C_0 we will consider are

$$M_0^- = \{(I, T, S) \in C_0 \mid f = 0, I < I_-^*\}, \quad (2.13)$$

$$M_0^+ = \{(I, T, S) \in C_0 \mid f = 0, I > I_+^*\}. \quad (2.14)$$

Note that the right-hand side of both equations in (2.11) are smooth everywhere on the domains $I > I_+^*$ and $I < I_-^*$, away from the line $T = S$. Hence M_0^+ and M_0^- are piecewise smooth manifolds.

The case $c = 0$ will be discussed in §2.3.3; from here on, we assume $c > 0$. Then the condition $\partial f / \partial I \neq 0$ also suffices to ensure the existence of a smooth inverse $I(T)$ of (2.12) that expresses I in terms of T (through the inverse function theorem). An example is shown in Figure 2.1. Write

$$T_+(R) = -c^{-1}(\lambda_+ + R), \quad T_-(R) = -c^{-1}(\lambda_- + R) \quad (2.15)$$

for the R -dependent value of T at the ice bifurcation points as determined by (2.12), where λ_{\pm} are defined in (1.15). These are threshold values for the meridional temperature difference T that, once crossed, lead to tipping of the ice component. Write $I = I_+(T)$ and $I = I_-(T)$ for the inverse of (2.12) when $I > I_+^*$ and $I < I_-^*$, respectively. Recall from §2.2 that $I > I_+^*$ and $I < I_-^*$ are equivalent to $T > T_+(R)$ and $T < T_-(R)$, respectively. Hence we

find that

$$M_0^- = \{(I, T, S) \in C_0 \mid I = I_-(T), T < T_-(R)\}, \quad (2.16)$$

$$M_0^+ = \{(I, T, S) \in C_0 \mid I = I_+(T), T > T_+(R)\}, \quad (2.17)$$

when $c \neq 0$. In the following two subsections, we will consider the flow on each of M_0^+ and M_0^- separately, before considering the whole slow system in §2.4. We will compare the flow on each of the slow manifolds to the Stommel flow (1.7), whose bifurcation structure was analysed in §1.2. Recall that the Stommel system has either one or two stable equilibria; in the on-regime, the temperature gradient T is larger than the salinity gradient S and the absolute flow rate $|\Psi|$ is large, and in the off-regime the salinity gradient dominates but the absolute flow rate is small. In conclusion, there are in total four possible stable equilibria: ice-on and ocean-on – also abbreviated to ion-on equilibrium, or denoted by $X_{\text{ion}}^{\text{on}}$; ice-on and ocean-off (ion-off, $X_{\text{ion}}^{\text{off}}$); ice-off and ocean-on (ioff-on, $X_{\text{ioff}}^{\text{on}}$); and ice-off and ocean-off (ioff-off, $X_{\text{ioff}}^{\text{off}}$).

2.3.1 The slow manifold M_0^-

On the slow manifold M_0^- – the ice-free regime – the flow simplifies further as there is no more sea ice to affect the evolution of T (see (2.11)). That is, the slow flow equals the Stommel flow (1.7), whose bifurcation structure was analysed in §1.2. As the flow on M_0^- is decoupled of the ice system, the number of equilibria (T^*, S^*) and their type solely depends on whether $T^* < T_-(R) = -c^{-1}(\lambda_- + R)$, i.e. whether $R + cT^* < -\lambda_-$. The line $R + cT^* = -\lambda_-$ thus separates two regions in the R, c -plane where T^* either does or does not exist. Denote by $T_{\text{ioff}}^{\text{on}}$ and $T_{\text{ioff}}^{\text{off}}$ the T -coordinate of the ioff-on and ioff-off equilibria. The two lines

$$L_{\text{ioff}}^{\text{off}} : R + cT_{\text{ioff}}^{\text{off}} = -\lambda_- \quad (2.18)$$

and

$$L_{\text{ioff}}^{\text{on}} : R + cT_{\text{ioff}}^{\text{on}} = -\lambda_- \quad (2.19)$$

are drawn in Figure 2.2(a), which shows the number of equilibria on M_0^- for $\hat{\eta}_1 = 3.0$, $\hat{\eta}_2 = 1.0$, and $\hat{\eta}_3 = 0.3$. Since $T_{\text{ioff}}^{\text{on}} < T_{\text{ioff}}^{\text{off}}$ and $T_-(R)$ decreases when R increases, the sole equilibrium in the blue shaded region is the ice-off, ocean-on equilibrium.

2.3.2 The slow manifold M_0^+

The polar ocean is ice-covered ($I > 0$) on the slow manifold M_0^+ , and hence the flow (2.11) depends on I . Nevertheless, there is still a relation between M_0^+ and the standard Stommel model (1.7). Indeed, suppose that T^*, S^* is an equilibrium of the slow flow (2.11), i.e. $\dot{T} = \dot{S} = 0$ in $T = T^*, S = S^*$. Then $I = I_+(T^*) =: I^*$ is also a fixed value. The standard

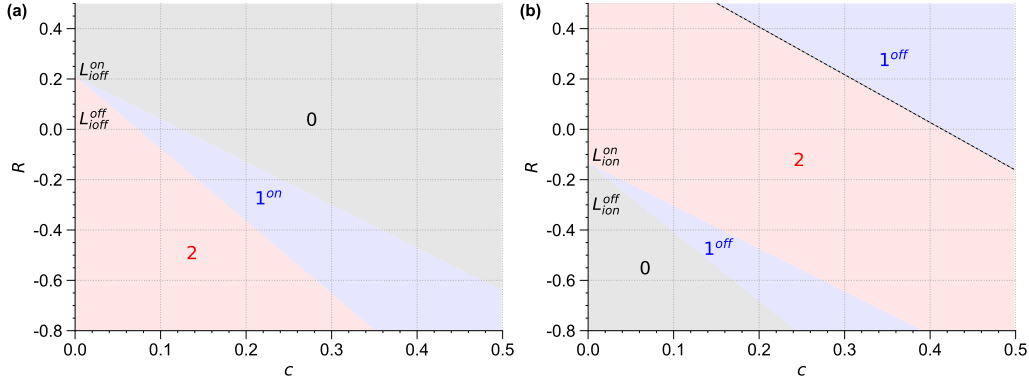


Figure 2.2: (a) Number of stable equilibria on the slow manifold M_0^- as a function of $c > 0$ and R when $\hat{\eta}_1 = 3.0$, $\hat{\eta}_2 = 1.0$, and $\hat{\eta}_3 = 0.3$. (b) Number of stable equilibria on the slow manifold M_0^+ as a function of $c > 0$ and R when $\hat{\eta}_1 = 3.0$, $\hat{\eta}_2 = 1.0$, $\hat{\eta}_3 = 0.3$, and $\kappa = 0.151$. The dashdotted line is L_{sn} , see (2.22). The decorated L 's in the figure refer to the other region-separating lines discussed in the text, see (2.18), (2.19), (2.20), (2.21). The colored numbers indicate the amount of fixed points that lie on the slow manifold in the respective shaded regions. Superscripts indicate the type of the existing oceanic state.

Stommel model (1.7) with $\eta_1 = \hat{\eta}_1 - \kappa I^*$, $\eta_2 = \hat{\eta}_2$ and $\eta_3 = \hat{\eta}_3$ must therefore also feature an equilibrium at $T = T^*$, $S = S^*$. The transient states do not coincide in theory, but Figure 2.3 demonstrates for a few practical examples that the difference between the basin boundaries for these two models is small.

Figure 2.2(b) shows the number of equilibria on M_0^+ as a function of R and c for $\kappa = 0.151$, again with $\hat{\eta}_1 = 3.0$, $\hat{\eta}_2 = 1.0$, and $\hat{\eta}_3 = 0.3$. The figure is now divided in four regions, as opposed to the three regions shown in Figure 2.2(a). Let $T_{\text{ion}}^{\text{off}}$ denote the T -coordinate of the ion-off state when $I = I_+^*$. Similar to before, the line

$$L_{\text{ion}}^{\text{off}} : R + cT_{\text{ion}}^{\text{off}} = -\lambda_+ \quad (2.20)$$

separates the region where no stable equilibria exist from the region where only the ion-off state exists. The line

$$L_{\text{ion}}^{\text{on}} : R + cT_{\text{ion}}^{\text{on}} = -\lambda_+ \quad (2.21)$$

(where $T_{\text{ion}}^{\text{on}}$ denotes the T -coordinate of the ion-on state when $I = I_+^*$) separates the lower region where only the off-state exists from the region of bistability. Both of these lines thus demarcate tipping of the ice cover, just as the two lines in Figure 2.2(a). However, the last visible border in Figure 2.2(b), that separates the region of bistability from the upper region where only the oceanic off-state exists, is due to crossing of the oceanic saddle-node bifurcation point, as $\hat{\eta}_1 - \kappa I^*$ there becomes smaller than $\eta_1^{\text{sn}} \approx 2.549$. That border is thus

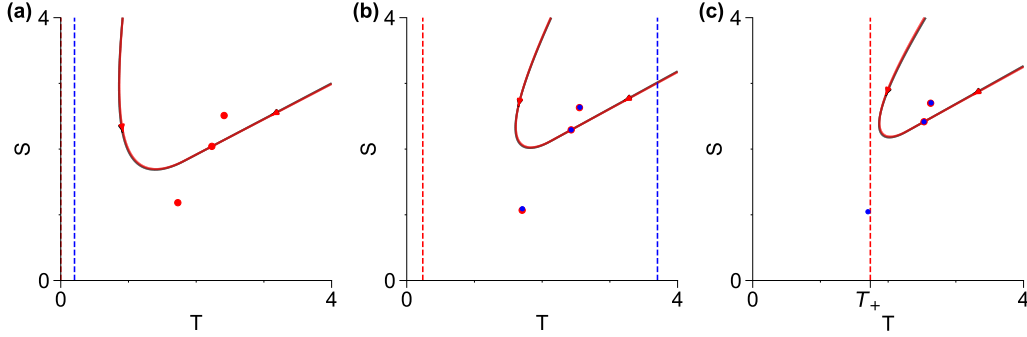


Figure 2.3: Basin boundary of the Stommel model (black) and of the reduced slow system in the ice-covered regime (red) in T - S phase space with $c = 0.1$ and $\kappa = 0.151$, for three values of R : (a) $R = R_{\text{ion}}^{\text{off}} + 0.6$, (b) $R = R_{\text{ion}}^{\text{off}} + 0.25$, (c) $R = R_{\text{ion}}^{\text{off}} + 0.1$. The dots are the equilibria of the ice-covered regime (red) and ice-free regime (blue) if they exist. The vertical, dashed lines are the temperature thresholds $T_+(R)$ (red) and $T_-(R)$ (blue). Here, $\hat{\eta}_1 = 3.0$, $\hat{\eta}_2 = 1.0$, and $\hat{\eta}_3 = 0.3$ for the reduced slow system; for the Stommel model, the parameters used are $\eta_1 = \hat{\eta}_1 - \kappa I(T^{\text{sa}})$, $\eta_2 = \hat{\eta}_2$, and $\eta_3 = \hat{\eta}_3$. Here, T^{sa} is the T -coordinate of the saddle equilibrium of the reduced slow system in the ice-covered regime. The basin boundary of the Stommel model is close to invisible because it almost coincides with the basin boundary of the reduced slow system. The red dot is the saddle point in both the Stommel model and in the reduced slow system.

the line

$$L_{\text{sn}}: R + cT^{\text{sn}} = -\lambda_{\text{sn}}, \quad (2.22)$$

where

$$\lambda_{\text{sn}} = \Delta \tanh(I^{\text{sn}}) + (R_0 - B)I^{\text{sn}} \quad \text{with} \quad I^{\text{sn}} = \frac{\hat{\eta}_1 - \eta_1^{\text{sn}}}{\kappa}.$$

As I^{sn} must be larger than I_+^* , we notice in addition that bistability can only exist when $\kappa < \frac{\hat{\eta}_1 - \eta_1^{\text{sn}}}{I_+^*}$, which is approximately 0.650 for $\hat{\eta}_1 = 3.0$. In addition, note that all three of $T_{\text{ion}}^{\text{off}}$, $T_{\text{ion}}^{\text{on}}$ and T^{sn} (and therefore also the associated lines) depend on κ .

Panel (a) in Figure 2.4 shows a bifurcation diagram of the flow on the slow manifold M_0^+ for $c = 0.1$, which is comparable to the bifurcation diagram of the Stommel model shown in Figure 1.2. Nevertheless, the equilibrium values of T , S and Ψ as a function of $\hat{\eta}_1$ also depend on the choice of c , as shown in Figure 2.4(b); notice the shift of the horizontal axis. We observe that the bistability area becomes a bit wider as c increases.

2.3.3 The case $c = 0$

At $c = 0$ the function f defined in (2.1) no longer depends on T , i.e. the feedback of the temperature gradient T in the ice equation ceases to exist. Therefore, the system (1.17) is coupled in only one direction. The constraint $f(I, T) = 0$ on the slow flow (2.11) no

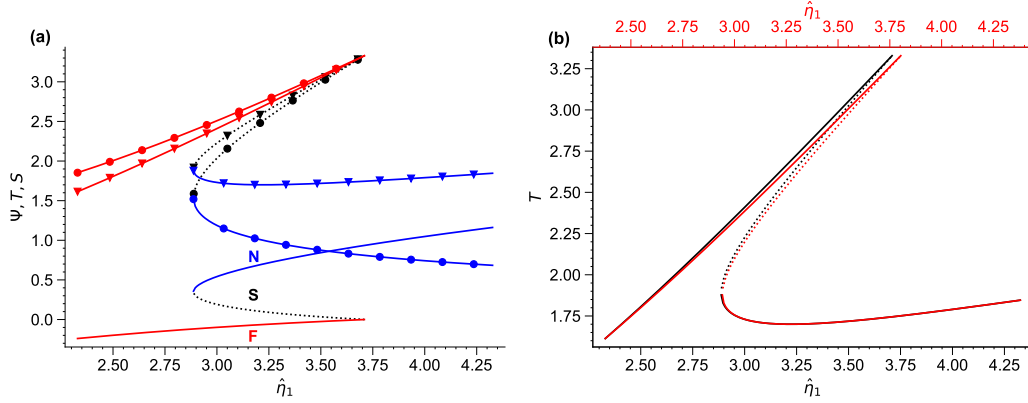


Figure 2.4: Bifurcation diagram of the slow flow on M_0^+ as $\hat{\eta}_1$ varies, with $\hat{\eta}_2 = 1.0$ and $\hat{\eta}_3 = 0.3$, $R = 0.2$, and $\kappa = 0.151$ fixed. Solid (dotted) lines indicate stable (unstable) equilibrium points. **(a)** Ψ (unmarked), T (triangles) and S (dots) for $c = 0.1$. The colored letters N, S and F indicate that the branches of that color are nodes, saddles, and foci. **(b)** T (unmarked) for $c = 0.1$ (black) and $c = 0.2$ (red). The bottom axis corresponds to the black graph, whereas the top axis corresponds to the red graph. The top axis is shifted compared to the bottom axis in order to make the increase of the width of the bistability area with increasing c visible.

longer depends on T as well. This means that I is constant for constant R . The number of equilibria on M_0^- and M_0^+ thus depends on the value of the $\hat{\eta}_i$ and whether R is small (or large) enough to support equilibria where the polar ocean is ice-free (or ice-covered). Hence M_0^- has two stable equilibria when $R < -\lambda_-$ and none otherwise. The slow flow on M_0^+ features two stable equilibria when $-\lambda_+ < R < -\lambda_{sn}$, one when $R \geq -\lambda_{sn}$, and none otherwise, consistent with Figure 2.2.

2.4 Bifurcation structure as R varies

Figure 2.5 shows the total number of stable equilibria present in the slow reduced system for the default value $\kappa = 0.151$ and for $\kappa = 0.303$. The additional value of $\kappa = 0.303$ is chosen so that the two values are representative for a wider range: a numerical calculation shows that any value of $\kappa < 0.240 \dots$ ensures $\lambda_{sn} < \lambda_-$ and the corresponding figure of stable equilibria resembles that of $\kappa = 0.151$; values of κ between $0.240 \dots$ and $\frac{\hat{\eta}_1 - \eta_1^{sn}}{I^*} \approx 0.650$ yield $\lambda_- < \lambda_{sn} < \lambda_+$, so that the associated figure of stable equilibria will resemble that of $\kappa = 0.303$. Note that the values of T_{ion}^{off} and T_{ion}^{on} (which are the slopes of the lines L_{ion}^{off} and L_{ion}^{on}) also depend on κ , but the variations in their values are not so large that they will significantly affect the figure of stable equilibria for the range of shown c -values, as long as λ_{sn} is not too close to either λ_+ or λ_- .

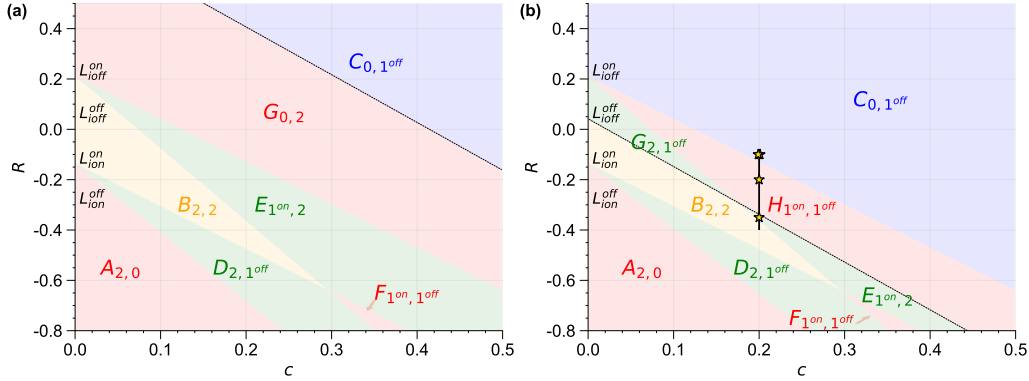


Figure 2.5: Number of stable equilibria of the reduced slow system (2.11) as a function of c and R when $\hat{\eta}_1 = 3.0$, $\hat{\eta}_2 = 1.0$, $\hat{\eta}_3 = 0.3$ and for (a) $\kappa = 0.151$ and (b) $\kappa = 0.303$. The letters are used in the text to refer to the various regions, whereas their subscripts are pairs (k, l) , where k and l are the number of stable equilibria on M_0^- and M_0^+ , respectively; in case only one equilibrium exists on M_0^- (or M_0^+), the type of the existing equilibrium is indicated in the superscript of k (or l). The color of each region is determined by the total amount $k + l$ of fixed points that lie in the region. The dashdotted line is L_{sn} , see (2.22). The decorated L 's in the figure refer to the other region-separating lines discussed in the text, see (2.18), (2.19), (2.20), (2.21). The black vertical line segment at $c = 0.2$ with the stars at $R = -0.35$, -0.2 , and -0.1 is relevant for the simulations performed in §3.1; see the caption of Figure 3.1.

Both panels feature the five region-separating lines $L_{i^{off}}^{off}$, $L_{i^{off}}^{on}$, L_{ion}^{off} , L_{ion}^{on} , and L_{sn} defined in §2.3.1 and §2.3.2. The presence of each of the four stable equilibria in each region may thus be assessed in relation to the region's location with respect to the five lines. Furthermore, as each of the lines except L_{sn} represents tipping of ice, Figure 2.5 shows where the system state can end up after tipping. For example, suppose we are at the ioff-off state at $c = 0.1$ and $R = -0.2$ (region B in both panels) and start increasing R . When $\kappa = 0.303$ (see Fig. 2.5(b)), the ioff-off equilibrium persists in region G but tips to the ion-off state in region H. By contrast, when $\kappa = 0.151$, Figure 2.5(a) is not conclusive about the fate of the ioff-off state when it reaches the green region E. In this case, we can appeal to a phase diagram such as in Figure 2.7(c), which shows that the ioff-off equilibrium for $\hat{\eta}_1 = 3.0$ falls within the basin of attraction of the ion-off state after tipping.

Figure 2.6 shows the types of transitions between different stable equilibria occurring in the slow system for $\kappa = 0.151$ and $\kappa = 0.303$. More precisely, this overview was made by checking at each boundary between regions in Figure 2.5 which equilibrium disappears, and in which basin of attraction the system lands afterwards if it would start at the disappearing equilibrium in the marginally stable state (if necessary by appealing to the associated phase diagram). Suppose as an example that the system starts in the marginally stable ice-off, ocean-off equilibrium in region B for $\kappa = 0.151$. When R increases, the ioff-off equilibrium



Figure 2.6: Transitions of the slow flow for $\kappa = 0.151$ (left) and $\kappa = 0.303$ (right) for $-0.8 \leq R \leq 0.5$ and $0 \leq c \leq 0.5$, as inferred from Figure 2.5 (see main text for explanation). In both cases, tipping from ion-off to ioff-on can only happen as a rate-dependent effect as discussed in §2.5. In the case $c = 0$ of unidirectional coupling, for both $\kappa = 0.151$ and $\kappa = 0.303$, tipping from ion-on to ioff-on and from ion-off to ioff-off happen ‘at BA’ (i.e. when moving from region B into region A in Fig. 2.5). For $\kappa = 0.151$, tipping from ioff-on to ion-on and from ioff-off to ion-off occur at BG. Lastly, the ocean-only tipping from ion-on to ion-off occurs at GC. For $\kappa = 0.303$, tipping from ioff-off to ion-off and from ioff-on to ion-off occurs at GC. The ocean-only tipping from ion-on to ion-off occurs at BG. When $c > 0$, for both $\kappa = 0.151$ and $\kappa = 0.303$, tipping from ion-on to ioff-on happen at BD and EF, and from ion-off to ioff-off happen at DA. For $\kappa = 0.151$, tipping from ioff-on to ion-on happens at EG, and from ioff-off to ion-off at BE and DF. The ocean-only tipping from ion-on to ion-off occurs at GC. For $\kappa = 0.303$, tipping from ioff-on to ion-off occurs at HC, and tipping from ioff-off to ion-off at GH and DF. Lastly, the ocean-only tipping from ion-on to ion-off happens at EH and BG. Tipping from ion-off to ioff-on (red arrows) happens at BA for $c = 0$ and at DA for $c > 0$, but only as a nonautonomous effect and when $\kappa < \kappa_R \approx 0.365$ (see §2.5 and §3.3). Therefore, the red arrows do not represent bifurcations that occur in (1.17).

disappears in a bifurcation of the ice component when moving into region E. Hence the system moves to the ice-covered regime. In a phase diagram it can be checked that the system lands in the basin of attraction of the ion-off state (compare Fig. 1.4 and Fig. 2.3).

Vertical arrows in Figure 2.6 represent ice-only transitions, horizontal arrows represent ocean-only transitions, and diagonal arrows represent cascading transitions where both ice and ocean tip. The types of transitions that can occur for $c = 0$ (i.e. when the model features only a unidirectional coupling) and for $c > 0$ are the same.

Figures 2.7, 2.8, 2.9, 2.10 provide diagrams of T – S phase space of the slow flow for $\kappa = 0.151$ and $\kappa = 0.303$ at $c = 0.1$ and $c = 0.2$ as R varies. Here, for a fixed value of c , we denote by e.g. $R_{\text{ion}}^{\text{off}}$ the value of R so that $(c, R_{\text{ion}}^{\text{off}})$ lies on the line $L_{\text{ion}}^{\text{off}}$. Figures A.1 and A.2 in the appendix show the same figures but for $\kappa = 0.38$.

2.5 Nonautonomous version

In the present-day, anthropogenic forcing has led to unprecedented rates of change in many key climate variables, and many subsystems of the climate are far out of equilibrium. Rate-dependent effects, where the climate system response depends on the rate at which climate parameters change, could therefore occur. In this section, we explore how the

dynamics of the coupled ocean-sea ice model changes when $R = R(t)$ is time-dependent as well, and discuss under which conditions the fast-slow analysis carried out in this chapter still applies. The nonautonomous version of the model (1.17) that we obtain in this way is

$$\begin{cases} I' = f(I, T, R), \\ T' = \epsilon g_1(I, T, S), \\ S' = \epsilon g_2(T, S), \\ R' = \delta h(R, t), \end{cases} \quad (2.23)$$

where $\tau_R = \delta^{-1}$ is the typical timescale of variations in R and $h(R, t)$ is a function of R and time t that is assumed to be sufficiently (piece-wise) smooth and of order 1 with respect to δ . From (2.15) we deduce

$$\frac{dT_+(R)}{dt} = \frac{dT_-(R)}{dt} = -c^{-1} \frac{dR}{dt}, \quad (2.24)$$

i.e. the threshold moving rate is fully determined by c and the rate of change of R . Generically, the system (2.23) features three different timescales, and whether it is comparable to the autonomous system (2.4) where R is treated as a parameter depends on the size of δ as compared to ϵ . That is, whether the fast-slow analysis carried out in this chapter still applies to the nonautonomous system depends on the rate of change of R as compared to that of I , T and S .

There are four different regimes to consider. First, if $\delta \ll \epsilon$, then the timescale of R is very large compared to the oceanic timescale. As R varies, the ocean-ice system state will thus adjust almost fully to the moving equilibrium. This regime is therefore comparable to the autonomous case where R is treated as a control parameter, as in the preceding sections. Second, when $\delta = O(\epsilon)$, the timescale of R mixes with the oceanic timescale, and the system trajectory may depend sensitively on the exact value of δ ; these rate-dependent effects will be discussed in §3.3. Third, when $\epsilon \ll \delta \ll 1$, variations in R will be almost instantaneous from the point of view of the oceanic timescale, which has little time to adjust. Lastly, when $\delta = O(1)$ or $\delta \gg 1$, the timescale of R is comparable to or even smaller than the timescale of the sea ice. Hence the fast-slow analysis performed in this chapter no longer holds, because R should now also be treated as a fast variable. The parameter R represents changes in the general circulation affecting the sea ice concentration, and a timescale comparable to or even smaller than that of sea ice thus seems unrealistic.

In Chapter 3, we will look into simulations of the nonautonomous model (2.23), and compare results for the first three regimes discussed above.

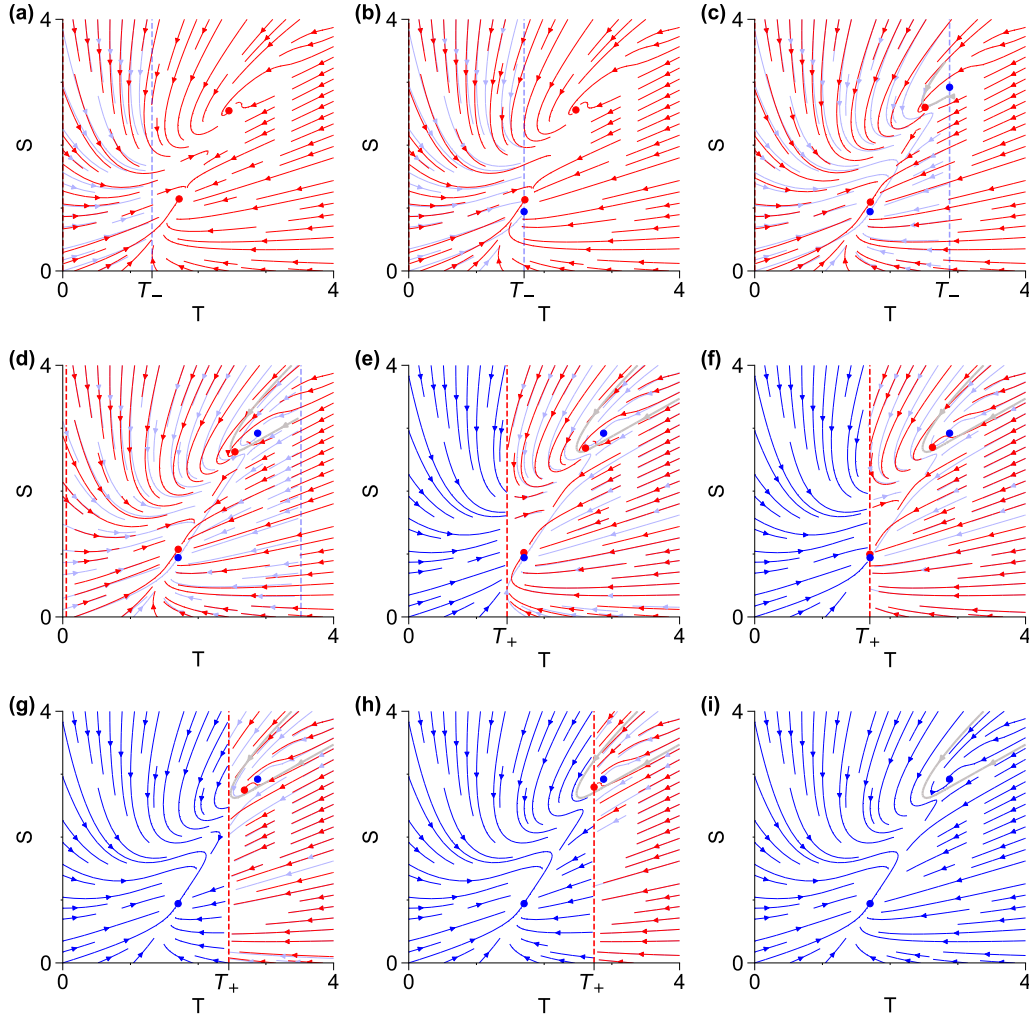


Figure 2.7: T - S phase space of the slow flow, with ice-covered (red) and ice-free (blue) regimes with borders given by the thresholds $T = T_+(R)$ (dashed red vertical line) and $T = T_-(R)$ (dashed blue vertical line), respectively, for nine decreasing values of R , with $\hat{\eta}_1 = 3.0$, $\hat{\eta}_2 = 1.0$, $\hat{\eta}_3 = 0.3$, $\kappa = 0.151$, and $c = 0.1$. Shown in light-blue is the part of the ice-free manifold for which the T -coordinate lies between $T_+(R)$ and $T_-(R)$. The basin boundary of the ioff-off equilibrium (grey) is drawn in some of the panels, obtained by backward integration of the saddle equilibrium of the ice-free system. **(a)** $R = 0.08$; only the ice-covered equilibria exist. **(b)** $R = R_{\text{ioff}}^{\text{on}} \approx 0.041$; the ioff-on equilibrium emerges as $T_-(R) = T_{\text{ioff}}^{\text{on}}$. **(c)** $R = R_{\text{ioff}}^{\text{off}} \approx -0.076$; the ioff-off equilibrium emerges as $T_-(R) = T_{\text{ioff}}^{\text{off}}$. **(d)** $R = -0.14$; **(e)** $R = -0.28$; **(f)** $R = R_{\text{ion}}^{\text{on}} \approx -0.305$; The ion-on equilibrium collides with the threshold $T = T_+(R)$ and disappears (the ioff-on equilibrium has almost the same T -coordinate, but is not affected here). **(g)** $R = -0.38$; **(h)** $R = R_{\text{ion}}^{\text{off}} \approx -0.408$; The ion-off equilibrium collides with the threshold $T = T_+(R)$ and disappears. **(i)** $R = -0.7$.

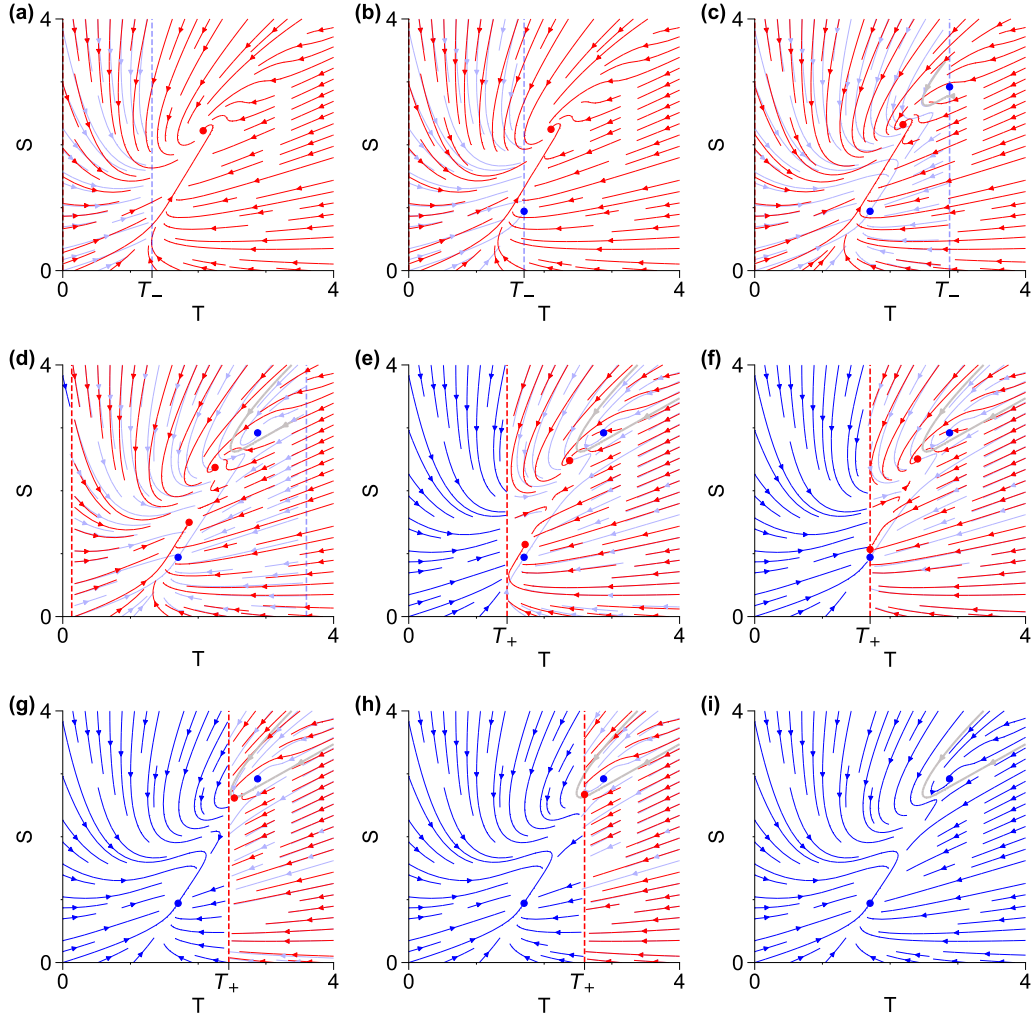


Figure 2.8: Same as Figure 2.7, but $\kappa = 0.303$ and $c = 0.1$. (a) $R = 0.08$; only the ion-off equilibrium exists. (b) $R = R_{\text{ion}}^{\text{on}} \approx 0.041$; the ion-off-on equilibrium emerges as $T_-(R) = T_{\text{ion}}^{\text{on}}$. (c) $R = R_{\text{ion}}^{\text{off}} \approx -0.076$; the ion-off-off equilibrium emerges as $T_-(R) = T_{\text{ion}}^{\text{off}}$. (d) $R = R^{\text{sn}} \approx -0.148$; The ion-on equilibrium emerges as the ice equilibrium value is now small enough for oceanic bistability to return. (e) $R = -0.28$; (f) $R = R_{\text{ion}}^{\text{on}} \approx -0.305$; The ion-on equilibrium collides with the threshold $T = T_+(R)$ and disappears (the ion-off-on equilibrium has almost the same T -coordinate, but is not affected here). (g) $R = -0.38$; (h) $R = R_{\text{ion}}^{\text{off}} \approx -0.408$; The ion-off equilibrium collides with the threshold $T = T_+(R)$ and disappears. (i) $R = -0.7$.

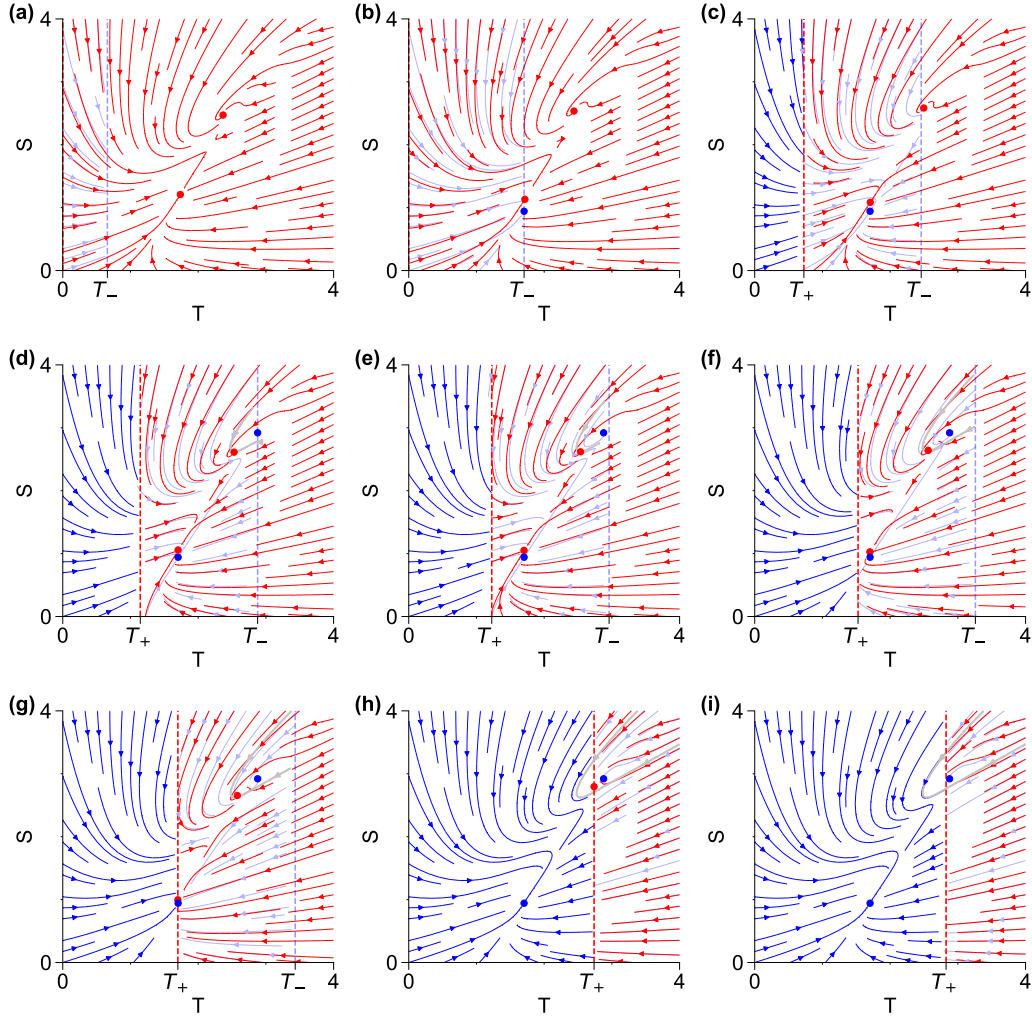


Figure 2.9: Same as Figure 2.7, but $\kappa = 0.151$ and $c = 0.2$. **(a)** $R = 0.08$; only the ice-covered equilibria exist. **(b)** $R = R_{\text{ioff}}^{\text{on}} \approx -0.129$; the ioff-on equilibrium emerges as $T_-(R) = T_{\text{ioff}}^{\text{on}}$. **(c)** $R = -0.28$; **(d)** $R = R_{\text{ioff}}^{\text{off}} \approx -0.364$; the ioff-off equilibrium emerges as $T_-(R) = T_{\text{ioff}}^{\text{off}}$. **(e)** $R = -0.38$. **(f)** $R = -0.44$. **(g)** $R = R_{\text{ion}}^{\text{on}} \approx -0.475$; The ion-on equilibrium collides with the threshold $T = T_+(R)$ and disappears (the ioff-on equilibrium has almost the same T -coordinate, but is not affected here). **(h)** $R = R_{\text{ion}}^{\text{off}} \approx -0.682$; The ion-off equilibrium collides with the threshold $T = T_+(R)$ and disappears. **(i)** $R = -0.7$.

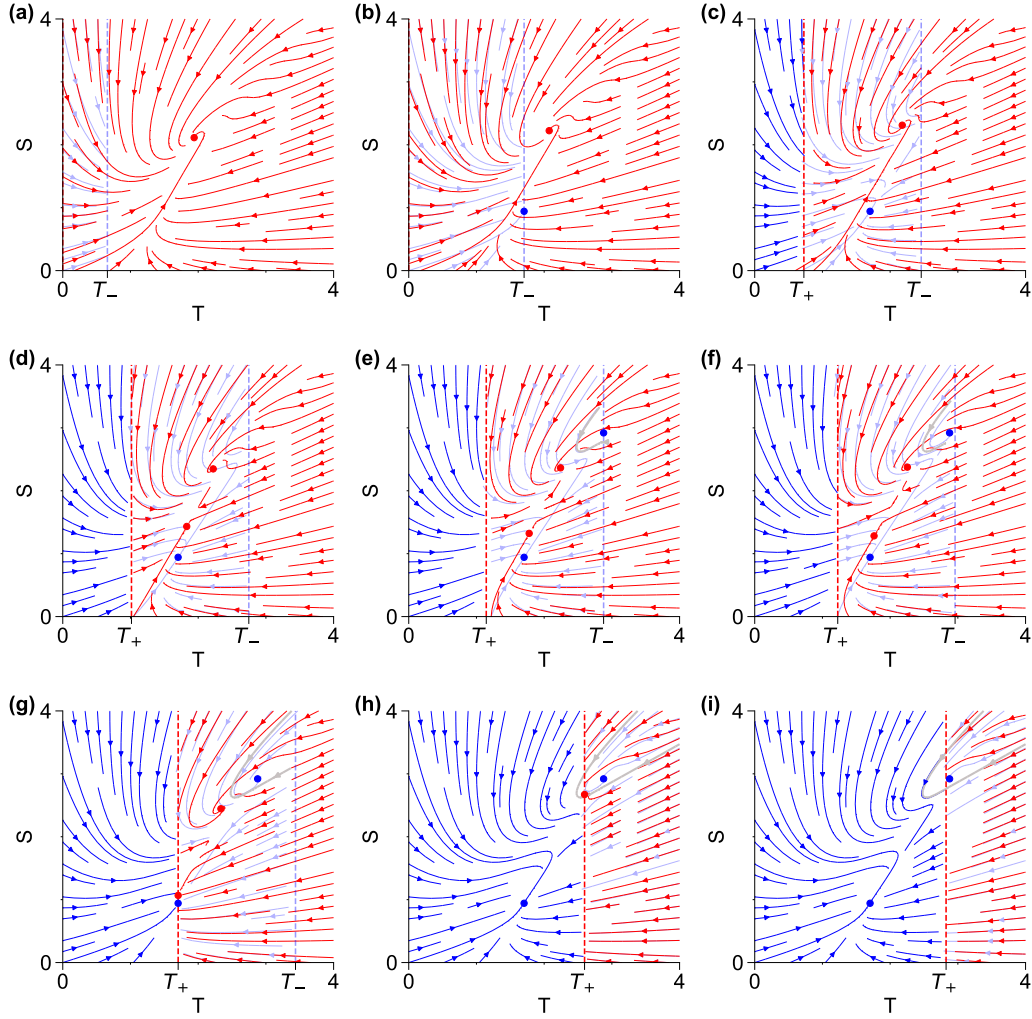


Figure 2.10: Same as Figure 2.7, but $\kappa = 0.303$ and $c = 0.2$. **(a)** $R = 0.08$; only the ion-off equilibrium exists. **(b)** $R = R_{\text{ion}}^{\text{on}} \approx -0.129$; the ioff-on state emerges as $T_-(R) = T_{\text{ion}}^{\text{on}}$. **(c)** $R = -0.28$; **(d)** $R = R^{\text{sn}} \approx -0.338$; The ion-on equilibrium emerges as the ice equilibrium value is now small enough for oceanic bistability to return. **(e)** $R = R_{\text{ion}}^{\text{off}} \approx -0.364$; the ioff-off equilibrium emerges as $T_-(R) = T_{\text{ion}}^{\text{off}}$. **(f)** $R = -0.38$. **(g)** $R = R_{\text{ion}}^{\text{on}} \approx -0.476$; The ion-on equilibrium collides with the threshold $T = T_+(R)$ and disappears (the ioff-on equilibrium has almost the same T -coordinate, but is not affected here). **(h)** $R = R_{\text{ion}}^{\text{off}} \approx -0.654$; The ion-off equilibrium collides with the threshold $T = T_+(R)$ and disappears. **(i)** $R = -0.7$.

Simulations

In this chapter, we study the full, bidirectionally coupled system (1.17) through simulations of the nonautonomous model (2.23) where R is decreased or increased between two points in time at a constant rate δ , and stays constant afterwards. In accordance with [22], we set the ocean-to-sea ice timescale ratio as $\tau_O = 200$, so that $\epsilon = \frac{1}{200} = 0.005$ (but the results are qualitatively similar for larger values of ϵ). All simulations were carried out using Euler forward for time integration with timesteps of 0.01 yr. The outcome of the simulations is compared to results from the fast-slow analysis carried out in Chapter 2.

In §3.1, we investigate how typical simulations of the nonautonomous system (2.23) where $\delta \ll \epsilon \ll 1$ compare to the fast-slow analysis carried out in Chapter 2. This leads to two examples of simulations where two transitions occur, which are analyzed in §3.2. Both of these transitions are not rate-dependent. In contrast, §3.3 showcases the rate-dependent cascading tipping point (where $\delta = O(\epsilon)$) discussed in [22], and demonstrates its existence in the bidirectionally coupled model (2.23) and in a nonautonomized version of the more extensive model (1.16).

3.1 Testing the fast-slow analysis

According to Figure 2.5(b), four different stable equilibria exist of (1.17) for $\kappa = 0.303$ at $c = 0.2$ and $R = -0.4$ (see region B). Figure 3.1 shows how these four equilibria respond to an increase in the parameter R at a fixed rate $\delta = 0.0003 \ll \epsilon$ to a fixed value R_{end} , depending on the simulation (see the caption).

Figure 3.1(c) shows how the ion-off state tracks the moving equilibrium while R increases, starting at $t = 800$ years after initialisation, until it hits $R_{\text{end}} = -0.1$. This is in accordance with Figure 2.5(b), that shows the ion-off equilibrium does not disappear for these values of R .

In the other simulation runs, the equilibria are lost due the parameter shift. As R increases, the first equilibrium to disappear is the ioff-off state (moving into region E in Fig. 2.5(b)). The simulation in Figure 3.1(a), where R is ramped up to $R_{\text{end}} = -0.35$,

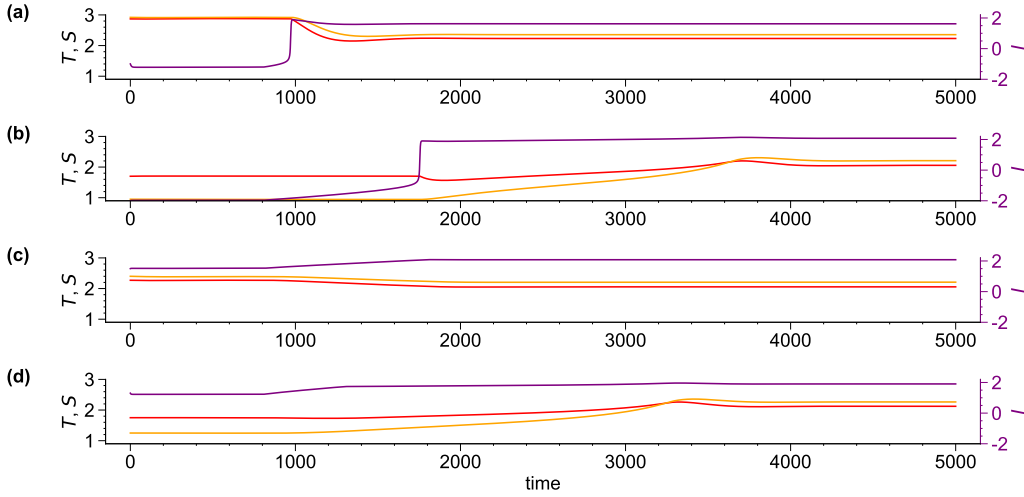


Figure 3.1: Simulations of the full, coupled system (2.23) with $c = 0.2$ and $\kappa = 0.303$ when R increases from -0.4 to R_{end} at a rate $\delta = 0.0003 \ll \epsilon$ starting from the (a) ice-off, ocean-off equilibrium ($R_{\text{end}} = -0.35$), (b) ice-off, ocean-on equilibrium ($R_{\text{end}} = -0.1$), (c) ice-on, ocean-off equilibrium ($R_{\text{end}} = -0.2$), and (d) ice-on, ocean-on equilibrium ($R_{\text{end}} = -0.1$). Shown are time series of T (red), S (orange) (left y-axis) and I (purple, right y-axis). The trajectories of R are represented in Figure 2.5(b) by the black vertical line segment at $c = 0.2$, with the stars denoting the various values of R_{end} .

indeed shows that the system tips to the ion-off state due to a bifurcation in the ice system. Although the ion-on state also exists for this combination of values of R and c , the system falls in the basin of attraction of the oceanic-off state after the ice component tips (see Fig. 2.10(h)).

Similarly, Figure 3.1(d) (where $R_{\text{end}} = -0.2$) shows that the ion-on state disappears due to a bifurcation in the ocean component (Fig. 2.5(b), region H; also see Fig. 2.10(b)-(d)). The system again converges to the ion-off state, in accordance with Figure 2.5(b).

Lastly, Figure 3.1(b) shows the trajectory of the ioff-on equilibrium, where again $R_{\text{end}} = -0.1$, that (as in Fig. 3.1(a)) also loses its stability through a saddle-node bifurcation of the ice component. However, here tipping of the ice cover is followed by tipping of the ocean state, albeit at a much slower rate. This is again in accordance with Figure 2.5(b), that shows only the oceanic-off state remains in the ice-covered regime for $R = -0.1$ (region C). The difference in tipping mechanism with Figure 3.1(d) is discussed further in §3.2.

In summary, all simulations end in the ion-off state due to tipping of the ice and/or ocean component, in accordance with Figure 2.5(b) and the theory from Chapter 2. For these values of ϵ and δ , the behaviour of the coupled system (2.23) is consistent with the dynamics of the slow flow discussed §2.3.

3.2 Two examples of two transitions

The transitions shown in Figure 3.1(b) are again depicted in Figure 3.2(b) and (d). The rate of change δ of R is increased tenfold in the latter compared to the former, so that $\delta = O(\epsilon)$. As a consequence, the ocean system cannot keep up with the moving equilibrium (see Fig. 3.2(c)). The same behaviour – ice tipping followed by ocean tipping – is observed nevertheless, consistent with Figure 2.5(b).

Figure 3.3(b) and (d) shows a similar transition, again starting from the ioff-on equilibrium, but for $\kappa = 0.151$ (note the larger simulation time). For purpose of illustration, here $\delta = 0.06 \gg \epsilon$. The simulation ending in the ion-off equilibrium (solid line) is complemented by one that ends in the ion-on state (dotted), that does exist in this case, in agreement with Figure 2.5(a). Therefore, tipping in the ocean system state in Figure 3.3 is not due to tipping of the ice, but rather in the subsequent further increase of the control parameter R . On the other hand, tipping toward the ice-covered regime means that the ocean component becomes dependent on I through the term $\eta_1 - \kappa\mathcal{H}(I)I$ in (1.17). As R increases further, I increases as well, and $\eta_1 - \kappa\mathcal{H}(I)I$ becomes so small that the ocean is pushed out of its bistable regime. Hence tipping toward the ice-covered regime enables the possibility of a bifurcation in the ocean component at a later stage.

In summary, qualitatively, the manifolds M_0^+ (see §2.3.2) for $\kappa = 0.151$ and $\kappa = 0.303$ differ at the moment of tipping of the ice cover in that only one equilibrium exists in the latter case, but two equilibria in the former (compare Fig. 2.5(a), region G, with Fig. 2.5(b), region C). For ocean tipping toward the off-state, tipping toward the ice-covered regime is a sufficient condition when $\kappa = 0.303$ (Fig. 3.2), but only a necessary condition when $\kappa = 0.151$ (Fig. 3.3).

Lastly, we discuss the effect of the rate of change δ of R as compared to ϵ on the trajectory of T and I . Figure 3.2(a) and (c) depict these trajectories in their bifurcation diagrams. Note that I closely tracks its stable state before and after tipping, whereas T is thrown far away from its equilibrium value (horizontal line from $\eta_1 - \kappa\mathcal{H}(I)I = 3.0$ to 2.4) when the ice cover tips, before slowly recovering. This is comparable to the trajectory shown in Figure 3.3(c), even though δ is much larger in the latter. The increase in δ is more visible when comparing the trajectories of I (Fig. 3.2(a) and Fig. 3.3(a)); in the latter also I cannot keep up with the environmental changes. Nevertheless, the final system states in Figure 3.2 and Figure 3.3 is independent of the rate of change δ of R .

3.3 Rate-dependent cascading tipping point

In this section, we consider the rate-dependent cascading tipping point discussed by Lohmann et al. [22, §3.3, Fig. 10] (see §1.4 for a comparison of our model with theirs). This contrasts with all previous transitions discussed, which are rate-independent.

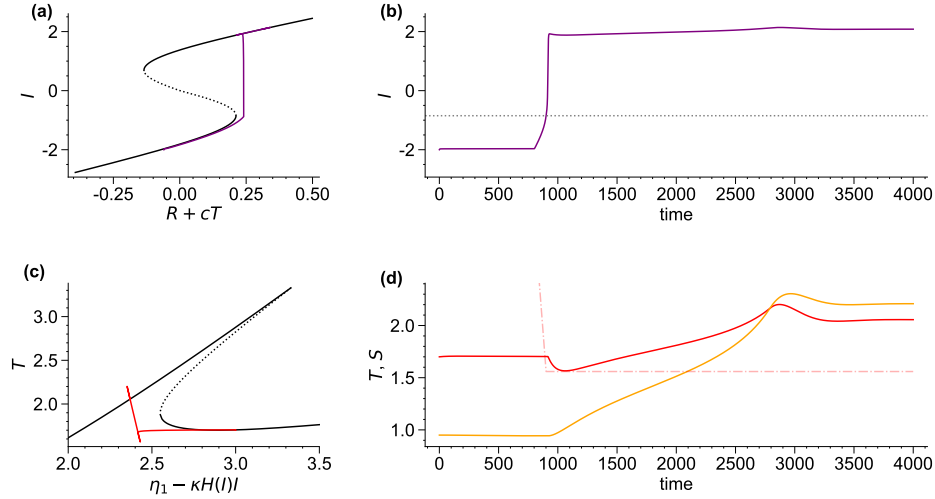


Figure 3.2: Ice tipping followed by ocean tipping from the ioff-on to the ion-off state in the coupled ocean-sea ice system, when the control parameter R is ramped up starting at $t = 800$ yr from $R = -0.4$ to $R = -0.1$ (solid) at a rate $\delta = 0.003 = O(\epsilon)$ with $\kappa = 0.303$ and $c = 0.2$. Here, ocean tipping is unavoidable once the ice cover has tipped. **(a)** Trajectory of I (purple), drawn in its bifurcation diagram with respect to $\hat{R} = R + cT$. **(b)** Time series of I . The horizontal, grey, dotted line indicates the ice tipping point value I_0^- . **(c)** Trajectory of T , drawn in its bifurcation diagram with respect to $\eta_1 - \kappa\mathcal{H}(I)I$. **(d)** Time series of T (red) and S (orange). The dashdotted, red line represents the moving threshold $T_-(R)$.

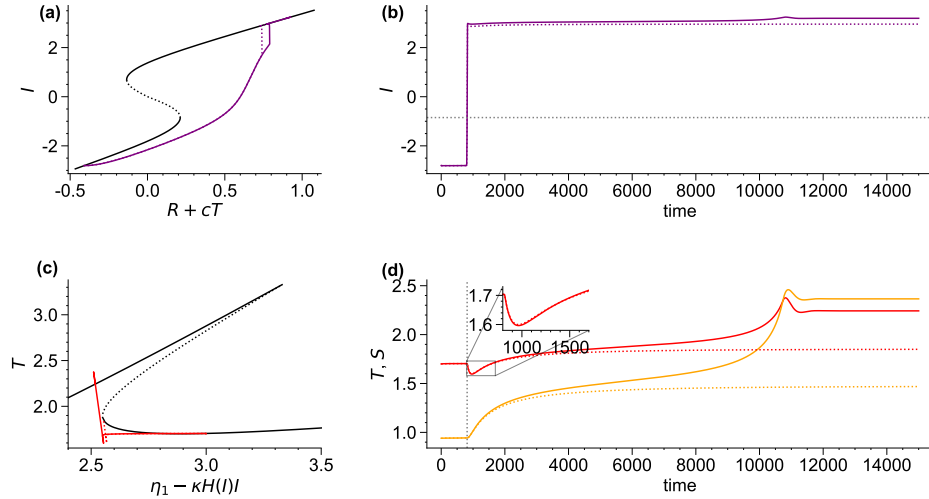


Figure 3.3: Ice tipping only (dashed) or ice tipping followed by ocean tipping (solid) starting from the ioff-on state in the coupled ocean-sea ice system, when the control parameter R is ramped up starting at $t = 800$ yr from -0.75 to 0.45 (solid) or to 0.4 (dotted) at a rate $\delta = 0.06 \gg \epsilon$ with $\kappa = 0.151$ and $c = 0.2$. **(a)** Trajectory of I (purple), drawn in its bifurcation diagram (see Figure 1.5) with respect to $R + cT$ (see §2.2). **(b)** Time series of I . The horizontal, grey, dotted line indicates the value I_0^- . **(c)** Trajectories of T in its bifurcation diagram with respect to $\eta_1 - \kappa\mathcal{H}(I)I$. **(d)** Time series of T (red) and S (orange). The vertical, grey, dotted line indicates the time where $I = I_0^-$.

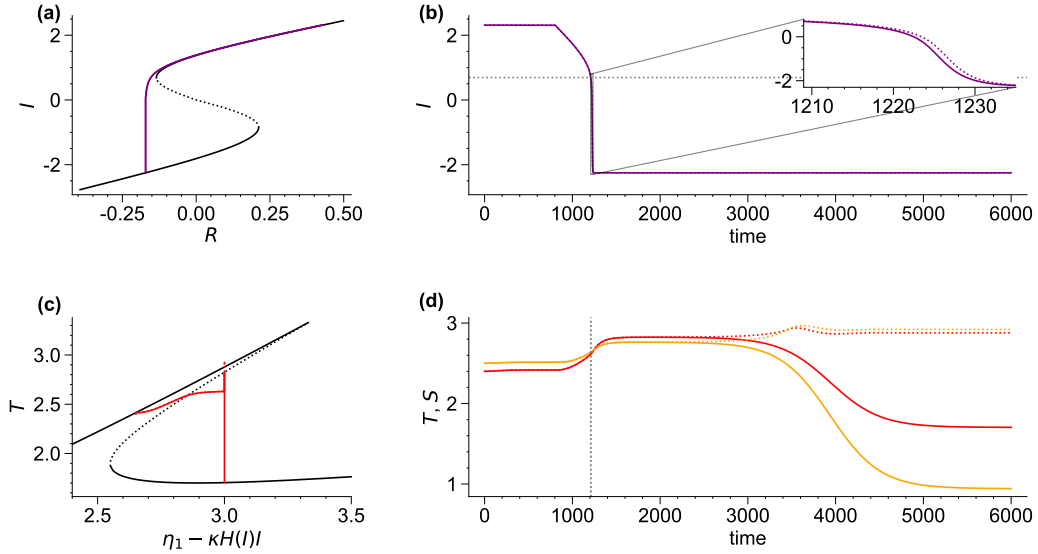


Figure 3.4: Rate-dependent cascading tipping point in the coupled ocean-ice system as in [22], i.e. with $c = 0$. From initial conditions $(T, S, I) = (2.4, 2.5, 2.312)$, with R ramped down from $3/7$ to $3/7 - 0.6$ over a duration of 422 years (solid) and 423 years (dotted) (i.e., $\delta \approx 0.0014$) starting at $t = 800$ yr, with $\kappa = 0.151$. **(a)** Trajectories of I (purple), drawn in its bifurcation diagram (black) with respect to R (see Figure 1.5). **(b)** Time series of I in the two simulations. The horizontal, grey, dotted line indicates the ice tipping point value I_0^+ . The inset illustrates that the two simulations follow a different trajectory. **(c)** Trajectories of T (red), drawn in its bifurcation diagram (black) with respect to $\eta_1 - \kappa\mathcal{H}(I)I$. **(d)** Time series of T (red) and S (orange). The vertical, grey, dotted line indicates the time where $I = I_0^+$.

Figure 3.4 demonstrates the difference in response of the coupled system to the same parameter shift occurring at slightly different rates. More precisely, it shows two simulation runs starting close to the ion-off equilibrium where, after a spin-up phase, the parameter R starts to decrease from $R \approx 0.42$ at time $t = 800$ yr at two slightly different rates close to $\delta = 0.0014 = O(\epsilon)$ (see caption for details), until it reaches $R \approx -0.17$. This guarantees a bifurcation-tipping of the ice component when R crosses $R_{\text{ion}}^{\text{off}} = -\lambda_+ \approx -0.13$.

Between $t = 800$ yr and approximately $t = 1210$ yr, the ice variable I stays close to its equilibrium value (Fig. 3.4(a)) as it decreases. The temperature gradient T , while increasing slightly, is still driven far out of equilibrium – see the part of Figure 3.4(c) where $\eta_1 - \kappa\mathcal{H}(I)I < 2.895$. Around $t = 1210$ yr, as R crosses the critical threshold $R_{\text{ion}}^{\text{off}} = -\lambda_+$ (Fig. 3.4(a)), the ice component quickly tips to the off-state (Fig. 3.4(b); inset). This leads to a rapid increase of $\eta_1 - \kappa\mathcal{H}(I)I$ to $\eta_1 = 3.0$. Hence \dot{T} becomes even more positive, so that T increases further.

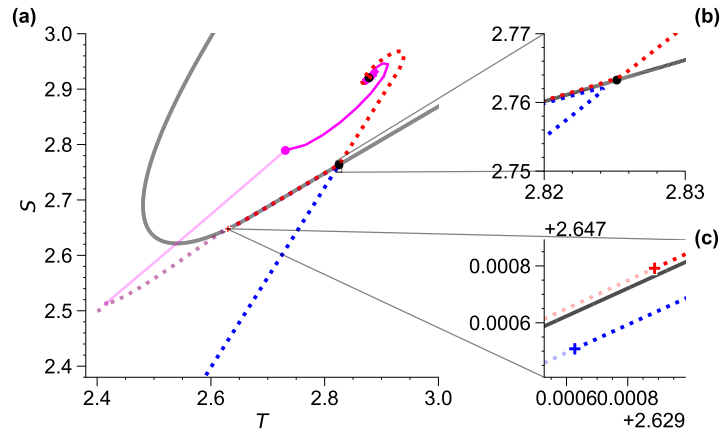


Figure 3.5: Trajectories (dotted) of the two simulations shown in Figure 3.4 in T - S phase space (blue corresponds to solid lines, red to dotted, in the latter figure). The grey curve is the boundary separating the basins of attraction of the ioff-off state (upper black dot) and the ioff-on state, or equivalently, the stable manifold of the saddle in the ice-free regime (lower black dot, on the basin boundary). The increase in opacity of the system trajectories reflect that the shown basin boundary is only the basin boundary of the system for $I < 0$. **(a)** Trajectory of the moving equilibrium while $I > 0$ (pink, transparent), and how the moving equilibrium would converge to the ioff-off state (pink, opaque) after ice tips to the off-state (pink dot). **(b)** Part of trajectories near the saddle (black dot) in the ice-free regime. **(c)** Part of trajectories and basin boundary at the moment that I becomes negative (plusses) in the respective simulation runs.

Up to now, the trajectories of the two different simulation runs have been virtually identical, and they remain so for an additional 1000 years (Fig. 3.4(d)). This is explained by the fact that both system trajectories, although never attracted by the saddle, do pass it closely before eventually converging to different equilibria, as can be seen in Figure 3.5(b). Nevertheless, their limit behaviour is already fully determined by the position of the ocean state with respect to the basin boundary of the ice-free regime at the exact moment that I becomes negative in the respective simulation runs. This is around year 1223 in both simulations (Fig. 3.4(b), inset). Indeed, as soon as I becomes smaller than zero, the ocean component decouples from the ice component and hence from any further change in R . Figure 3.5(c) shows that, indeed, the respective ocean system states lie on opposite sides of the basin boundary, implying that they will eventually converge to different equilibria.

Figure 3.5(a) also shows the trajectory of the moving equilibrium (pink, transparent) as R decreases. While $R > R_{\text{ion}}^{\text{off}}$, the ion-off state and moves in an almost straight line as R decreases. When $R = R_{\text{ion}}^{\text{off}}$ (pink dot), the ion-off equilibrium ceases to exist due to bifurcation tipping as $I = I_0^+$. If the system would be in this ion-off state, it would tip to the ice-free regime and follow the pink, opaque trajectory toward the ioff-off state.

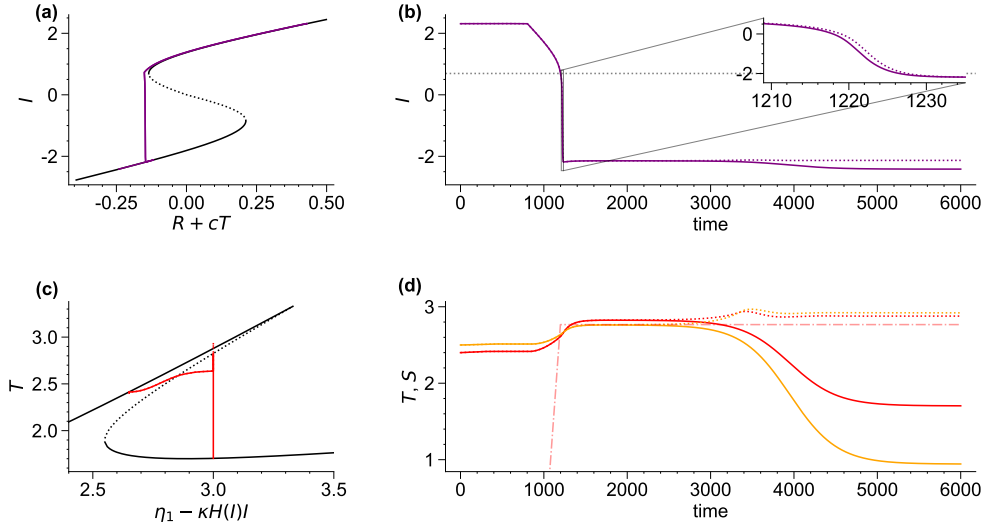


Figure 3.6: Simulations as in Figure 3.4, but with $c = 0.1$. From initial conditions $(T_0, S_0, I_0) = (2.4, 2.5, 2.312)$, with R ramped down from $3/7 - 0.24$ to $3/7 - 0.84$ over a duration of 397 years (solid) and 398 years (dotted) (i.e., $\delta \approx 0.0015$) with $\kappa = 0.151$. **(a)** Trajectory of I (purple), drawn in its bifurcation diagram (black) with respect to $\hat{R} = R + cT$ (see §2.2). **(b)** Time series of I . The horizontal, grey, dotted line indicates the ice tipping point value I_0^+ . **(c)** Trajectories of T drawn in its bifurcation diagram with respect to $\eta_1 - \kappa H(I)I$. **(d)** Time series of T (red) and S (orange). The red, dashdotted line indicates the temperature threshold $T_+(R)$.

The trajectory of the moving equilibrium has been established by appealing to the correspondence between equilibria in the ice-free and ice-covered regimes outlined in §2.3.2. In particular, the ion-off state with Stommel parameter $\hat{\eta}_1$ is equal to the ioff-off state with Stommel parameter $\eta_1 = \hat{\eta}_1 - \kappa I^*$, where I^* is the value of I in the ion-off equilibrium. As this correspondence depends on κ , the location of the ocean system when the ice component tips to the off-state (the pink dot in Figure 3.5) also depends on κ . Rate-dependent tipping can only occur as long as the pink dot lies in the basin of attraction of the ioff-off state, which can be calculated to be around $\kappa = \kappa_R \approx 0.365$. That is, when $\kappa > \kappa_R$, tipping of the ice cover will always lead to tipping of the ocean component as well, regardless of the rate of change of R . See Figure A.1 and Figure 2.10 for T - S phase space pictures when $\kappa = 0.38$ and $c = 0.1$ or $c = 0.2$; in both figures, panel (h) shows that the ion-off state will fall outside of the basin of attraction of the ioff-off equilibrium after R decreases further.

Figure 3.4(c) shows the trajectories of T in its bifurcation diagram. Both of them cross the dotted line indicating the saddle. Whereas the trajectory indicated by the solid line tips to the lower branch, signifying the AMOC-on state, the dotted trajectory still converges to the off-state. The same behaviour is shown when drawing the bifurcation diagram of

S with respect to $\eta_1 - \kappa\mathcal{H}(I)I$. This example serves to illustrate that the limit behaviour of the system cannot be read off from the trajectory in T - or S -bifurcation diagrams, as is suggested in [22, Fig. 4]; even more, ‘tracking’ or ‘tipping’ is not a consequence of crossing the basin boundary at some point during the parameter shift, but rather of the location of the ocean state with respect to the basin boundary at the moment that the ice component decouples of the ocean state, as explained above.

The size of δ at which rate-dependent cascading tipping emerges seems to be of order ϵ , regardless of the exact value of the latter. For example, when $\epsilon = 1/50$, simulations (not shown here) demonstrate that a rate-induced tipping point exists when the ramping duration is decreased to 91 or fewer years, so that $\delta \approx 0.0066$. The corresponding trajectory figure is very similar to Figure 3.5.

Figure 3.6 shows a rate-induced cascading tipping point of the fully coupled system (1.17) where $c = 0.1$. The initial value of R is chosen in such a way that the initial value of the state variable I is the same as in the simulation shown in Figure 3.4. Panel (d) in Figure 3.6 now also shows the movement of the temperatures threshold $T_+(R)$ over time, which is fully determined by the rate of change of R (see (2.24)).

The overall behaviour of the simulation runs is very comparable to the simulations shown for $c = 0$ in Figure 3.4. In the following, we will highlight only the differences.

First, notice that the lowest rate at which rate-induced tipping first occurs is slightly higher, but of the same order as in the unidirectionally coupled case (compare the captions of Figure 3.4 and Figure 3.6). This is ascribed to the slight increase in T when R is already decreasing but the ice component hasn’t tipped yet, effectively reducing the rate at which $R + cT$ decreases.

After the system has tipped into the ice-free regime, the feedback of the ice component into the ocean system disappears. However, the ice and ocean component do not decouple as the feedback of T into the ice component remains. Therefore, the ice system becomes the following system of the ocean system, and responds on the oceanic timescale to the adjustment of T to its new equilibrium. Hence the limit behaviour of I differs between the simulations, in contrast with the simulations for $c = 0$.

Figure 3.7 shows that the rate-dependent cascading tipping point also exists in the more elaborate system (1.16) where the term cT is replaced by $\bar{c}T_p$, requiring the introduction of a fourth equation. Although this would render a fast-slow analysis as in Chapter 2 more complicated, Figure 3.7 shows that similar behaviour is to be expected. In particular, panel (f) shows that the initial response of T_p to tipping of the ice cover has a much larger amplitude compared to T_e . This gives some justification for treating T_e as a constant, which is the assumption leading to (1.17).

Lastly, we discuss the possible rate-dependency of other tipping points in (1.17). In the example given in this section, the key characteristic that led to rate-dependency is the fact that the orbit of the moving equilibrium (Fig. 3.5(a), pink line) crosses the basin boundary

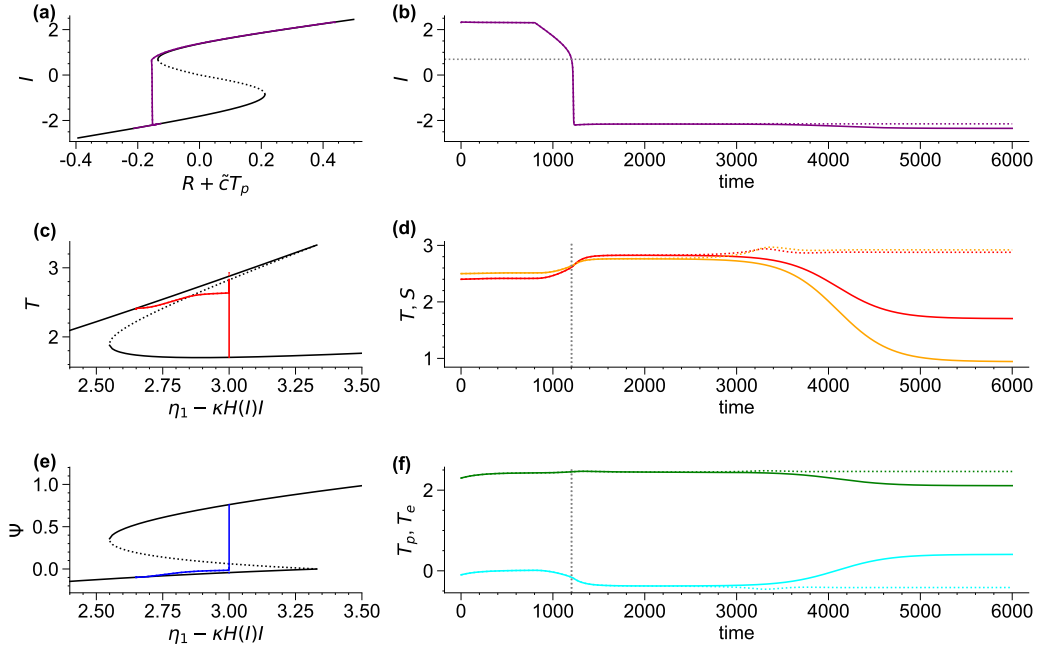


Figure 3.7: Rate-dependent cascading tipping point in the system (1.16), with $\tilde{c} = -0.1$, $T_p^a = -0.5$, $T_e^a = 2.5$, $\xi = 0.7$, $\kappa = 0.151$, $\epsilon = \tau_O^{-1} = 0.005$, from initial conditions $(T_{e,0}, T_{p,0}, S_0, I_0) = (2.3, -0.1, 2.5, 2.312)$, with R ramped down from $3/7$ to $3/7 - 0.6$ over a duration of 404 years (solid) and 405 years (dotted) (i.e., $\delta \approx 0.0015$) with $\kappa = 0.151$. (a) Trajectories of I (purple), drawn in its bifurcation diagram (black) with respect to $R + \tilde{c}T_p$. (b) Time series of I . The horizontal, grey, dotted line indicates the ice tipping point value I_0^+ . (c) Trajectories of T drawn in its bifurcation diagram with respect to $\eta_1 - \kappa\mathcal{H}(I)I$. (d) Time series of T (red) and S (orange). (e) Trajectories of Ψ (blue) drawn in its bifurcation diagram with respect to $\eta_1 - \kappa\mathcal{H}(I)I$. (f) Time series of T_p (cyan) and T_e (green).

of the underlying ice-free regime. If the trajectory in a simulation diverges enough from that of the moving equilibrium, it can end up at the other side of the basin boundary once it has tipped to the ice-free regime. We analyze if this process can occur under other circumstances. First, since the equilibria in the ice-free regime are not dependent on R , they stay fixed in time. Hence rate-dependency in tipping toward the ice-covered regime cannot occur, and the oceanic state never changes when sea ice returns. Second, the ion-on state can lose its stability in two processes: through an ocean bifurcation when R increases (which cannot be rate-dependent), or through a saddle-node bifurcation of the ice component when R decreases. In the latter case, the system will always tip toward the ion-on state, because the basin of attraction of the ion-on state fully contains the basin of attraction of the ion-off state (see Fig. 1.4 and Fig. 2.3). Hence only the ion-off state is susceptible to rate-dependent tipping.

Discussion and conclusion

In this thesis, we studied a bidirectionally coupled version of the conceptual AMOC-sea ice model proposed in [22]. Apart from extending the discussion on the mechanisms discussed in [22] for a rate-induced resurgence of the AMOC after disappearance of sea ice to the bidirectionally coupled case, we showed other cascading or ‘double’ transitions that can occur in this model. Here, we first comment on the classification of tipping points in open systems [3] in §4.1 and on the proposed classification of tipping cascades [16] in §4.2 before discussing the possible relevance of some of the observed tipplings to the climate system in §4.3. Lastly, we conclude with a discussion of possibilities for future research in §4.4, including limitations and possible extensions of the model formulation that may help in the investigation of types of transitions. Furthermore, we stress the importance of basin boundary considerations in general for coupled models.

4.1 R-tipping and B-tipping

A synthesis of different types of tipping – ‘classical’ bifurcation tipping (B-tipping), rate-dependent tipping points (R-tipping), and noise-induced tipping (N-tipping) – in the context of climate was first presented in [3]. Noise has not been considered in this thesis and will be left out of this discussion; however, see [22] for some results considering N-tipping in the model (1.17) with $c = 0$. In subsequent work [35], R-tipping is described as a ‘genuine nonautonomous instability’, i.e., a kind of tipping that is absent in the underlying autonomous model, but emerges when the nonautonomous model is considered. It should be noted that R-tipping for the autonomous model is B-tipping for the associated nonautonomous model, albeit a global bifurcation (which we haven’t encountered earlier in this thesis).

Let us analyze the rate-dependent cascading tipping point in the model (2.23) discussed in §3.3, where we start from the ice-on, ocean-off equilibrium and decrease the parameter R (with $c = 0.1$ and $\kappa = 0.151$; see Fig. 3.6). We think of the system trajectory in three-dimensional phase space, with respect to T , S , and I . The tipping occurs in two

stages. In the first stage, R is increased until it reaches the critical threshold $R_{\text{ion}}^{\text{off}}$. In the autonomous system (1.17), where R is treated as a control parameter, the moving ion-off equilibrium shifts toward a place (in the plane $I = I_+^*$) where its projection straight down to the plane $I = 0$ is a point lying inside the basin of attraction of the ion-off equilibrium (Fig. 3.5, pink dot). In the nonautonomous system (2.23), the system state trajectory diverges from the orbit of the moving equilibrium and may end up lying above either side of the basin boundary. However, the system state still lies well inside the basin of attraction of the ion-off equilibrium at $I = I_+^*$. In the second stage, R actually crosses the critical threshold $R_{\text{ion}}^{\text{off}}$, the ion-off equilibrium disappears, the variable I abruptly decreases to negative values, and in the nonautonomous state the trajectory of the system state can end up lying on either side of the basin boundary at $I \leq 0$ – yielding the rate-dependent tipping point in the ocean component. This description shows that the rate-dependent cascading tipping point is a combination of B-tipping (in the ice component) and R-tipping (in the ocean component); one cannot go without the other in the present system for practical examples, because the basin boundary is simply too far away before I reaches negative values (Fig. 1.4). Indeed, Figure 1.4 shows that the oceanic-off equilibria of the Stommel model for $\eta_1 \geq \eta_1^{\text{sn}}$ lie within the basin of attraction of the Stommel model for $\eta_1 \leq 2.9$. As we have seen in Figure 2.3 that the basin boundary of the slow manifold virtually coincides with the associated basin boundary in the Stommel model, we conclude that there is a value of η_1 at most slightly smaller than 2.9 for which rate-dependent cascading tipping starting from the bistable regime cannot occur (for the values $\eta_2 = 1.0$ and $\eta_3 = 0.3$).

4.2 Classification of cascading tipping points

In [16], a classification of cascading tipplings in idealized conceptual models consisting of two subsystems with a bidirectional and linear coupling was proposed. The classification consists of three different types: a two phase cascade, a domino cascade, and a joint cascade. We explain the three types using the examples of cascading tipping described in Chapter 3. We note that the subsystems in [16] act on the same timescale, in contrast with the timescale separation between the sea ice and ocean subsystems in our case. Another obstacle to direct comparison is that the classification of [16] requires shifts in the control parameter to be slow enough such that the system tracks the moving equilibrium. Hence the rate-dependent cascading tipping point discussed in §3.3 does not fit into the classification. Nevertheless, a comparison with the classification can still be made for the two cascades discussed in §3.2 (in both of those cases, the system does track the moving equilibrium, in spite of the large value of δ compared to ϵ).

The transition in Figure 3.3 (solid lines) is an example of a two phase cascade, because tipping of the ocean component can be halted if the the parameter R does not increase too far (dotted lines), even after the ice cover has tipped to its on-state. In contrast, tipping

of the ocean component in Figure 3.2 is unavoidable once the ice component has tipped. This is because the shift in the value of R has already altered the background conditions for the ocean component in the ice-on state such that only the ocean-off equilibrium remains. In other words, only one stable state exists on the ice-on branch already prior to tipping (Fig. 2.10(c)). Therefore, this transition is a joint cascade. A domino cascade could only occur if tipping of ice cover itself would induce loss of one stable state in the ocean component, but this is not the case here.

4.3 Interpretation of tippings

The model (1.17) is capable of simulating a wide range of possible tippings, and in this thesis we have investigated the parameter space in depth. We showed that the rate-dependent cascading tipping point first discussed by Lohmann et al. [22] persists in the two-way coupled model. As outlined in the Introduction, this mechanism could have played a role in past DO events, where (in the first part of the DO cycle) a rapidly declining sea ice cover might have led to a strengthening of the AMOC. Figure 2.6 and Figure 2.5 show that transitions between the on- and off-states of the ocean can occur either as a rate-dependent effect as discussed in §3.3 above, or due to loss of oceanic bistability, possibly in combination with tipping of the ice cover.

Deterministic cascading tipping only exists from the ioff-on to the ion-off equilibrium (Fig. 2.6 and §3.2), and is avoidable (i.e. a two phase cascade) in case the coupling coefficient of the sea ice into the ocean component is not too large. This emphasizes the need for a good understanding of the strength of the coupling between the Arctic sea ice cover and the AMOC in past and future climates.

4.4 Conclusion and further research

In this thesis, we have extended the conceptual coupled model of [22] to include a two-way coupling and gave a fast-slow analysis of the resulting system to explain the tipping points that can occur in this model. It was shown that the same tipping points and cascades exist in our model as in [22], and that the fast-slow analysis captured simulations of the full model very well. Even with varying just a few parameters, it was shown that the model behaviour is already quite rich. The parameter values of the Stommel model have been kept fixed throughout. It is clear however that tipping behaviour could be quite different when those are varied as well, especially because of the changing basin boundary position with respect to the equilibria of the Stommel model. The concept of forward basin stability (see §1.2 and [35, §4.3]) is very important in this regard, and an intrinsic property of the Stommel model that might not exist in other, more extensive models of the AMOC.

The presence of the same rate-dependent cascading tipping point in the extended system (1.16), where cT is replaced by $\tilde{c}T_p$ (see Figure 3.7), suggests that (1.17) captures the behaviour of the former quite well. However, additional research is required to assess if this also holds for the overall behaviour of the model. More generally, it is unclear how well the bidirectional coupling introduced here actually represents feedback processes that occur in the polar ocean and in the AMOC (even as a conceptual model). Rather, in this thesis this conceptual model was used as a playground to see what changes when bidirectional coupling is introduced, and how a formal fast-slow analysis is carried out to support the observations made in [22].

It would be of great interest to extend this model with an atmospheric and land ice component and study if the ensuing multiple timescale dynamics (a very fast atmospheric component, a fast sea ice component, a slow ocean component, and a very slow land ice component) could generate full DO cycles, as already suggested in [22]. A simple approach could be to couple increases in R past a certain threshold with large freshwater input in the polar box, simulating the response from the Greenland ice sheet. This alone could for example suffice to push the system state outside of the basin of attraction of the oceanic-off state.

Supplementary material

In this chapter, we discuss the genericity of the chosen parameter values for the Stommel model, and also include a few additional figures. See https://github.com/davidhokken/ocean_seaice_tipping_thesis for code used to produce the figures and simulations in this thesis, as well as the figures themselves and a few movies.

Genericity of chosen parameter values for ocean component

Here, we show that the choice of Stommel parameters used in this thesis is at least somewhat generic, in the sense that for any choice of η_2 and $0 < \eta_3 < 1$ where the oceanic-off state exists, it will move in the right-upper direction for increasing η_1 . The right-upward movement of the stable oceanic-off equilibrium with increasing η_1 can be seen in Figure 1.4.

Suppose the system is in the equilibrium off-state of the Stommel model and keep η_2 and η_3 fixed. Then $|T - S| = S - T$. Again, we assume S and T are positive to mimic realistic conditions. Implicitly differentiating the expressions for T and S in (1.9) with respect to η_1 gives

$$1 = \frac{\partial \eta_1}{\partial \eta_1} = \frac{\partial}{\partial \eta_1}(T(1 + S - T)) = (1 + S - 2T)\frac{\partial T}{\partial \eta_1} + T\frac{\partial S}{\partial \eta_1} \quad (\text{A.1})$$

and

$$0 = \frac{\partial \eta_2}{\partial \eta_1} = \frac{\partial}{\partial \eta_1}(S(\eta_3 + S - T)) = (\eta_3 + 2S - T)\frac{\partial S}{\partial \eta_1} - S\frac{\partial T}{\partial \eta_1}. \quad (\text{A.2})$$

Combining these two expressions into one for $\frac{\partial T}{\partial \eta_1}$ gives

$$\frac{\partial T}{\partial \eta_1} = \left(1 + S - 2T + \frac{TS}{\eta_3 + 2S - T}\right)^{-1} = \frac{\eta_3 + 2S - T}{\eta_3 + (\eta_3 + 2)S - (2\eta_3 + 1)T + 2(S - T)^2}$$

which – using only that $S > T$ – is greater than 0 since $\eta_3 + 2S - T > \eta_3 + 2T - T = \eta_3 + T > 0$ and $(\eta_3 + 2)S - (2\eta_3 + 1)T > (\eta_3 + 2)T - (2\eta_3 + 1)T = (1 - \eta_3)T > 0$. Furthermore, from (A.2) we immediately see that also $\frac{\partial S}{\partial \eta_1} > 0$, but $\frac{\partial T}{\partial \eta_1} > \frac{\partial S}{\partial \eta_1}$. This means that at some point, the condition $S > T$ doesn't hold anymore. This is the case when $S = T$, i.e. when $T = \eta_1 = \eta_2/\eta_3 = S$ as per (1.9).

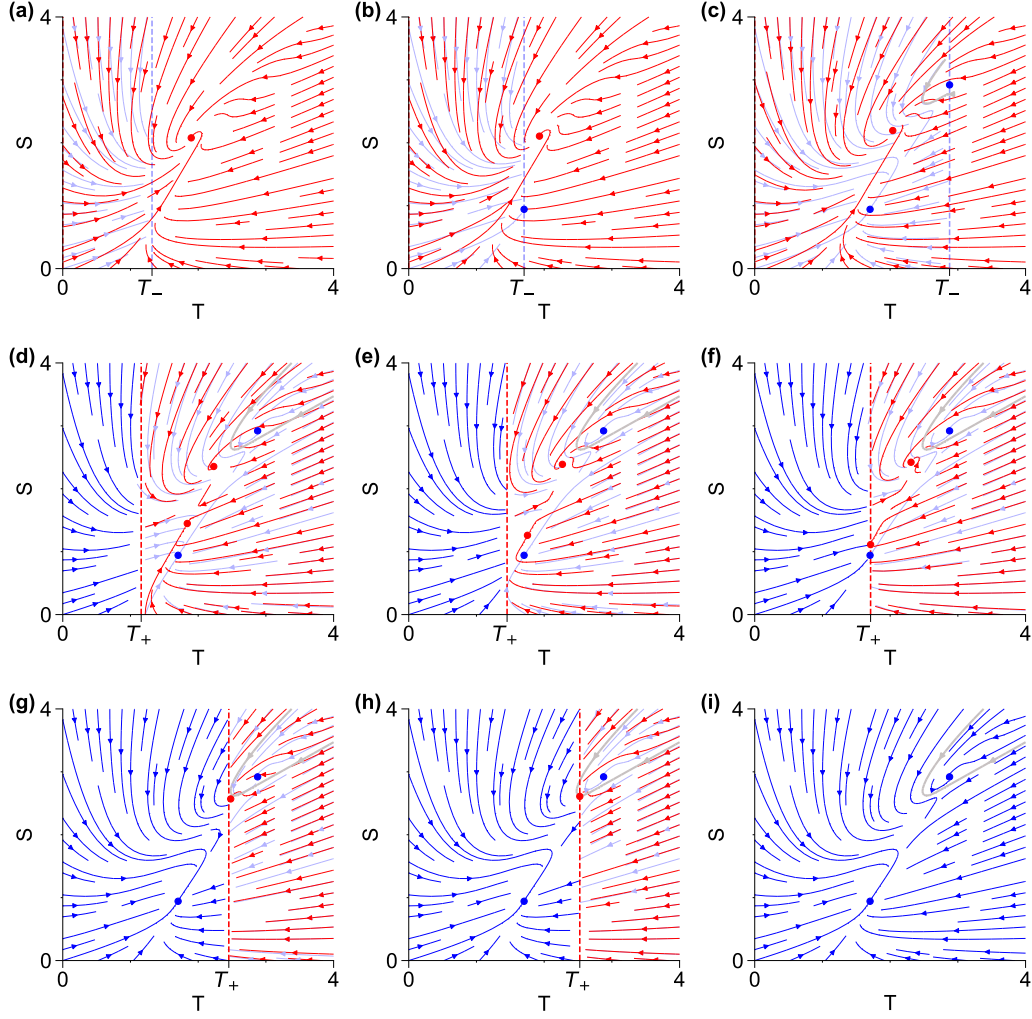


Figure A.1: Same as Figure 2.7, but $\kappa = 0.38$ and $c = 0.1$. **(a)** $R = 0.08$; only the ion-off state exists. **(b)** $R = R_{\text{ion}}^{\text{on}} \approx 0.041$; the ioff-on state emerges as $T_-(R) = T_{\text{ion}}^{\text{on}}$. **(c)** $R = R_{\text{ion}}^{\text{off}} \approx -0.076$; the ioff-off state emerges as $T_-(R) = T_{\text{ion}}^{\text{off}}$. **(d)** $R = R^{\text{sn}} \approx -0.251$; The ion-on state emerges as the ice equilibrium value is now small enough for oceanic bistability to return. **(e)** $R = -0.28$; **(f)** $R = R_{\text{ion}}^{\text{on}} \approx -0.306$; The ion-on state collides with the threshold $T = T_+(R)$ and disappears (the ioff-on state has almost the same T -coordinate, but is not affected here). **(g)** $R = -0.38$; **(h)** $R = R_{\text{ion}}^{\text{off}} \approx -0.387$; The ion-off state collides with the threshold $T = T_+(R)$ and disappears. **(i)** $R = -0.7$.

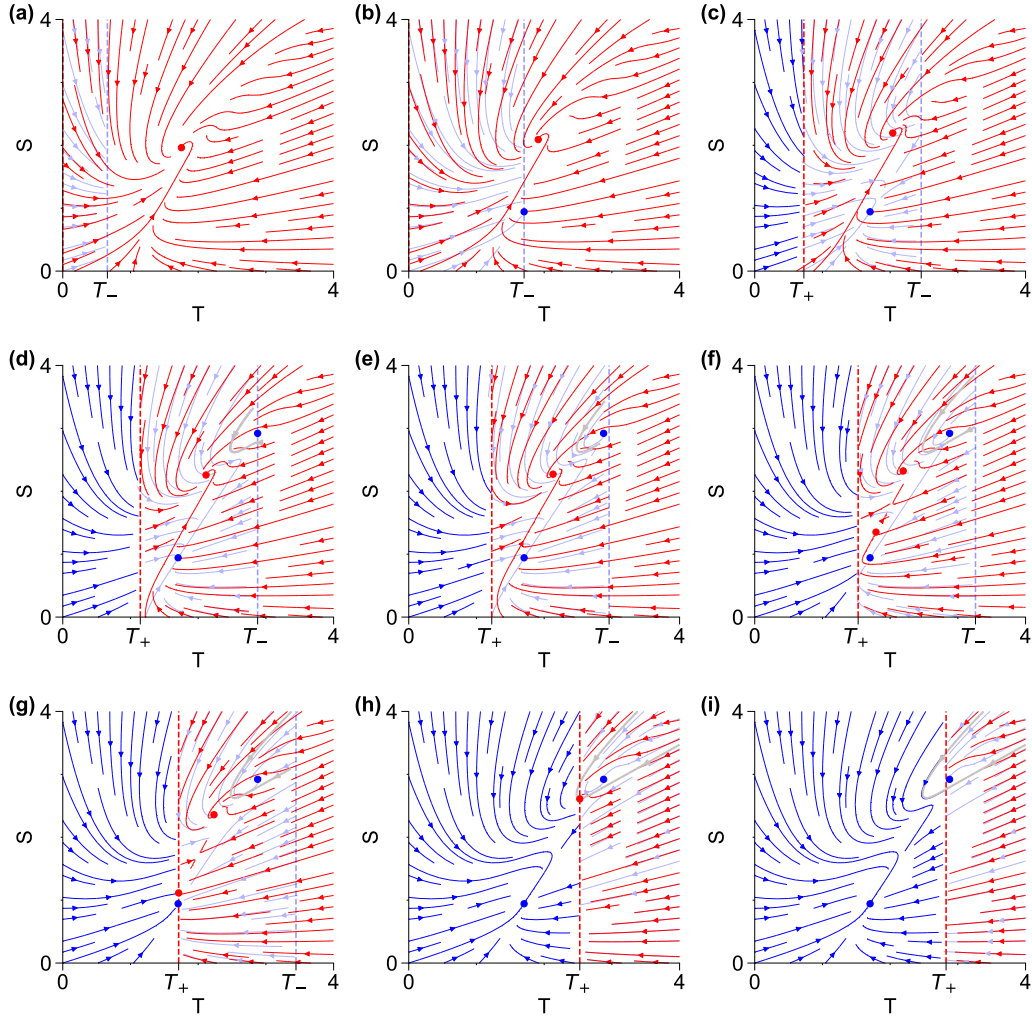


Figure A.2: Same as Figure 2.7, but $\kappa = 0.38$ and $c = 0.2$. **(a)** $R = 0.08$; only the ion-off state exist. **(b)** $R = R_{\text{ioff}}^{\text{on}} \approx -0.129$; the ioff-on state emerges as $T_-(R) = T_{\text{ioff}}^{\text{on}}$. **(c)** $R = -0.28$; **(d)** $R = R_{\text{ioff}}^{\text{off}} \approx -0.364$; the ioff-off state emerges as $T_-(R) = T_{\text{ioff}}^{\text{off}}$. **(e)** $R = -0.38$. **(f)** $R = R^{\text{sn}} \approx -0.440$; The ion-on state emerges as the ice equilibrium value is now small enough for oceanic bistability to return. **(g)** $R = R_{\text{ion}}^{\text{on}} \approx -0.477$; the ion-on state collides with the threshold $T = T_+(R)$ and disappears (the ioff-on state has almost the same T -coordinate, but is not affected here). **(h)** $R = R_{\text{ion}}^{\text{off}} \approx -0.640$; The ion-off state collides with the threshold $T = T_+(R)$ and disappears. **(i)** $R = -0.7$.

Bibliography

- [1] H. Alkhayuon, P. Ashwin, L. C. Jackson, C. Quinn, and R. A. Wood. *Basin bifurcations, oscillatory instability and rate-induced thresholds for Atlantic meridional overturning circulation in a global oceanic box model*. Proceedings of the Royal Society A **475** (2019), 20190051. doi: [10.1098/rspa.2019.0051](https://doi.org/10.1098/rspa.2019.0051).
- [2] P. Ashwin, C. Perryman, and S. Wicczorek. *Parameter shifts for nonautonomous systems in low dimension: bifurcation-and rate-induced tipping*. Nonlinearity **30** (2017), 2185. doi: [10.1088/1361-6544/aa675b](https://doi.org/10.1088/1361-6544/aa675b).
- [3] P. Ashwin, S. Wicczorek, R. Vitolo, and P. Cox. *Tipping points in open systems: bifurcation, noise-induced and rate-dependent examples in the climate system*. Philosophical Transactions of the Royal Society A: Mathematical, Physical and Engineering Sciences **370** (2012), 1166–1184. doi: [10.1098/rsta.2011.0306](https://doi.org/10.1098/rsta.2011.0306).
- [4] R. Bastiaansen, H. A. Dijkstra, and A. S. von der Heydt. *Fragmented tipping in a spatially heterogeneous world*. Environmental Research Letters **17** (2022), 045006. doi: [10.1088/1748-9326/ac59a8](https://doi.org/10.1088/1748-9326/ac59a8).
- [5] N. Boers, M. Ghil, and D. D. Rousseau. *Ocean circulation, ice shelf, and sea ice interactions explain Dansgaard–Oeschger cycles*. Proceedings of the National Academy of Sciences **115** (2018), E11005–E11014. doi: [10.1073/pnas.1802573115](https://doi.org/10.1073/pnas.1802573115).
- [6] M. M. Dekker, A. S. von der Heydt, and H. A. Dijkstra. *Cascading transitions in the climate system*. Earth System Dynamics **9** (2018), 1243–1260. doi: [10.5194/esd-9-1243-2018](https://doi.org/10.5194/esd-9-1243-2018).
- [7] H. A. Dijkstra. *Dynamical oceanography*. Springer Science & Business Media, 2008. doi: [10.1007/978-3-540-76376-5](https://doi.org/10.1007/978-3-540-76376-5).
- [8] H. A. Dijkstra. *Nonlinear climate dynamics*. Cambridge University Press, 2013. doi: [10.1017/CB09781139034135](https://doi.org/10.1017/CB09781139034135).
- [9] H. A. Dijkstra and M. Ghil. *Low-frequency variability of the large-scale ocean circulation: A dynamical systems approach*. Reviews of Geophysics **43** (2005). doi: [10.1029/2002RG000122](https://doi.org/10.1029/2002RG000122).
- [10] S. S. Drijfhout, S. Bathiany, C. Beaulieu, V. Brovkin, M. Claussen, C. Huntingford, M. Scheffer, G. Sgubin, and D. Swingedouw. *Catalogue of abrupt shifts in Intergovernmental Panel on Climate Change climate models*. Proceedings of the National Academy of Sciences **112** (2015), E5777–E5786. doi: [10.1073/pnas.1511451112](https://doi.org/10.1073/pnas.1511451112).
- [11] I. Eisenman. *Factors controlling the bifurcation structure of sea ice retreat*. Journal of Geophysical Research: Atmospheres **117** (2012). doi: [10.1029/2011JD016164](https://doi.org/10.1029/2011JD016164).

-
- [12] I. Eisenman and J. S. Wettlaufer. *Nonlinear threshold behavior during the loss of Arctic sea ice*. Proceedings of the National Academy of Sciences **106** (2009), 28–32. doi: [10.1073/pnas.0806887106](https://doi.org/10.1073/pnas.0806887106).
- [13] H. Gildor and E. Tziperman. *A sea ice climate switch mechanism for the 100-kyr glacial cycles*. Journal of Geophysical Research: Oceans **106** (2001), 9117–9133. doi: [10.1029/1999JC000120](https://doi.org/10.1029/1999JC000120).
- [14] G. A. Gottwald. *A model for Dansgaard–Oeschger events and millennial-scale abrupt climate change without external forcing*. Climate Dynamics **56** (2021), 227–243. doi: [10.1007/s00382-020-05476-z](https://doi.org/10.1007/s00382-020-05476-z).
- [15] IPCC. *Climate Change 2021: The Physical Science Basis. Contribution of Working Group I to the Sixth Assessment Report of the Intergovernmental Panel on Climate Change*. Ed. by V. Masson-Delmotte, P. Zhai, A. Pirani, S.L. Connors, C. Péan, S. Berger, N. Caud, Y. Chen, L. Goldfarb, M.I. Gomis, M. Huang, K. Leitzell, E. Lonnoy, J.B.R. Matthews, T.K. Maycock, T. Waterfield, O. Yelekçi, R. Yu, and B. Zhou. Cambridge University Press, Cambridge, United Kingdom and New York, NY, USA, In press, 2021. doi: [10.1017/9781009157896](https://doi.org/10.1017/9781009157896).
- [16] A. K. Klose, N. Wunderling, R. Winkelmann, and J.F. Donges. *What do we mean, 'tipping cascade'?* Environmental Research Letters (2021). doi: [10.1088/1748-9326/ac3955](https://doi.org/10.1088/1748-9326/ac3955).
- [17] C. Kuehn. *Multiple time scale dynamics*. Vol. 191. Springer, 2015. doi: [10.1007/978-3-319-12316-5](https://doi.org/10.1007/978-3-319-12316-5).
- [18] T. M. Lenton. *Tipping points in the climate system*. Weather **76** (2021), 325–326. doi: [10.1002/wea.4058](https://doi.org/10.1002/wea.4058).
- [19] T. M. Lenton, H. Held, E. Kriegler, J. W. Hall, W. Lucht, S. Rahmstorf, and H. J. Schellnhuber. *Tipping elements in the Earth's climate system*. Proceedings of the national Academy of Sciences **105** (2008), 1786–1793. doi: [10.1073/pnas.0705414105](https://doi.org/10.1073/pnas.0705414105).
- [20] C. Li, D. S. Battisti, D. P. Schrag, and E. Tziperman. *Abrupt climate shifts in Greenland due to displacements of the sea ice edge*. Geophysical Research Letters **32** (2005). doi: [10.1029/2005GL023492](https://doi.org/10.1029/2005GL023492).
- [21] C. Li and A. Born. *Coupled atmosphere-ice-ocean dynamics in Dansgaard-Oeschger events*. Quaternary Science Reviews **203** (2019), 1–20. doi: [10.1016/j.quascirev.2018.10.031](https://doi.org/10.1016/j.quascirev.2018.10.031).
- [22] J. Lohmann, D. Castellana, P. D. Ditlevsen, and H. A. Dijkstra. *Abrupt climate change as a rate-dependent cascading tipping point*. Earth System Dynamics **12** (2021), 819–835. doi: [10.5194/esd-12-819-2021](https://doi.org/10.5194/esd-12-819-2021).
- [23] G. A. Maykut and N. Untersteiner. *Some results from a time-dependent thermodynamic model of sea ice*. Journal of Geophysical Research **76** (1971), 1550–1575. doi: [10.1029/JC076i006p01550](https://doi.org/10.1029/JC076i006p01550).
- [24] P. E. O’Keeffe and S. Wiczorek. *Tipping phenomena and points of no return in ecosystems: beyond classical bifurcations*. SIAM Journal on Applied Dynamical Systems **19** (2020), 2371–2402. doi: [10.1137/19M1242884](https://doi.org/10.1137/19M1242884).
- [25] M. Rietkerk, R. Bastiaansen, S. Banerjee, J. van de Koppel, M. Baudena, and A. Doelman. *Evasion of tipping in complex systems through spatial pattern formation*. Science **374** (2021), eabj0359. doi: [10.1126/science.abj0359](https://doi.org/10.1126/science.abj0359).

- [26] J. C. Rocha, G. Peterson, Ö. Bodin, and S. Levin. *Cascading regime shifts within and across scales*. *Science* **362** (2018), 1379–1383. doi: [10.1126/science.aat7850](https://doi.org/10.1126/science.aat7850).
- [27] W. Steffen, J. Rockström, K. Richardson, T. M. Lenton, C. Folke, D. Liverman, C. P. Summerhayes, A. D. Barnosky, S. E. Cornell, M. Crucifix, et al. *Trajectories of the Earth System in the Anthropocene*. *Proceedings of the National Academy of Sciences* **115** (2018), 8252–8259. doi: [10.1073/pnas.1810141115](https://doi.org/10.1073/pnas.1810141115).
- [28] H. Stommel. *Thermohaline convection with two stable regimes of flow*. *Tellus* **13** (1961), 224–230. doi: [10.1111/j.2153-3490.1961.tb00079.x](https://doi.org/10.1111/j.2153-3490.1961.tb00079.x).
- [29] P. Valdes. *Built for stability*. *Nature Geoscience* **4** (2011), 414–416. doi: [10.1038/ngeo1200](https://doi.org/10.1038/ngeo1200).
- [30] G. K. Vallis. *Atmospheric and oceanic fluid dynamics*. Cambridge University Press, 2017. doi: [10.1017/9781107588417](https://doi.org/10.1017/9781107588417).
- [31] G. Walin. *The thermohaline circulation and the control of ice ages*. *Palaeogeography, palaeoclimatology, palaeoecology* **50** (1985), 323–332. doi: [10.1016/0031-0182\(85\)90075-6](https://doi.org/10.1016/0031-0182(85)90075-6).
- [32] W. Weijer, W. Cheng, S. S. Drijfhout, A. V. Fedorov, A. Hu, L. C. Jackson, W. Liu, E. L. McDonagh, J. V. Mecking, and J. Zhang. *Stability of the Atlantic Meridional Overturning Circulation: A review and synthesis*. *Journal of Geophysical Research: Oceans* **124** (2019), 5336–5375. doi: [10.1029/2019JC015083](https://doi.org/10.1029/2019JC015083).
- [33] W. Weijer, W. Cheng, O. A. Garuba, A. Hu, and B. T. Nadiga. *CMIP6 models predict significant 21st century decline of the Atlantic meridional overturning circulation*. *Geophysical Research Letters* **47** (2020), e2019GL086075. doi: [10.1029/2019GL086075](https://doi.org/10.1029/2019GL086075).
- [34] S. Wieczorek, P. Ashwin, C. M. Luke, and P. M. Cox. *Excitability in ramped systems: the compost-bomb instability*. *Proceedings of the Royal Society A: Mathematical, Physical and Engineering Sciences* **467** (2011), 1243–1269. doi: [10.1098/rspa.2010.0485](https://doi.org/10.1098/rspa.2010.0485).
- [35] S. Wieczorek, C. Xie, and P. Ashwin. *Rate-Induced Tipping: Thresholds, Edge States and Connecting Orbits*. 2021. doi: [10.48550/ARXIV.2111.15497](https://doi.org/10.48550/ARXIV.2111.15497).
- [36] N. Wunderling, J. F. Donges, J. Kurths, and R. Winkelmann. *Interacting tipping elements increase risk of climate domino effects under global warming*. *Earth System Dynamics* **12** (2021), 601–619. doi: [10.5194/esd-12-601-2021](https://doi.org/10.5194/esd-12-601-2021).